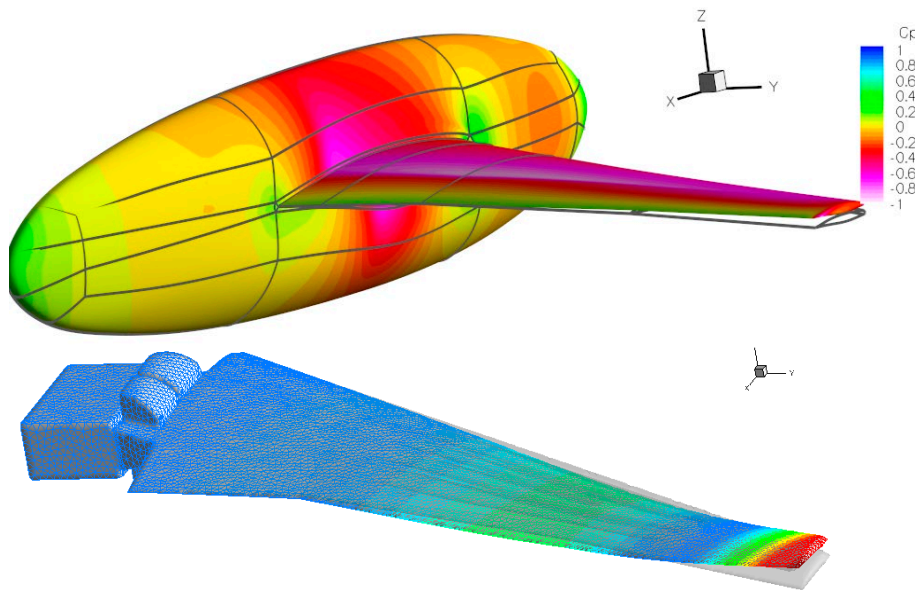




Executive summary

Transonic unsteady aerodynamic analysis of HIRENASD wing oscillating in flexible modes

Contribution to AIAA Aeroelastic Prediction Workshop I, Honolulu, USA, April 21-22, 2012



Report no.

NLR-TP-2012-476

Author(s)

B.B. Prananta
J. van Muijden
B.J.G. Eussen

Report classification

UNCLASSIFIED

Date

February 2013

Knowledge area(s)

Aëro-elasticiteit en
vliegtuigbelastingen
Computational Physics en
theoretische aërodynamica

Descriptor(s)

unsteady aerodynamics
transonic
flutter
oscillating wing

Problem area

One of the most critical tasks during the development and modification of an aircraft concerns the flutter clearance, i.e. ensuring that a catastrophic dynamic aeroelastic instability does not occur within the design flight envelope. In most cases, following the most common means of compliance to the regulation, the activities for flutter clearance culminate in a potentially dangerous flight flutter test. Reliable flutter analyses have to be carried out prior to the flight test campaign to ensure freedom from flutter and specifically to contribute to the success of the test.

Due to the nature of a flight flutter test, the flow condition imposed on the aircraft can be far off the cruise condition, i.e. at the boundary of the flight envelope. Complex flow phenomena can be expected to occur such as flow separation induced by shockwaves. Standard linear unsteady aerodynamic methods such as doublet lattice or kernel function methods can not model these phenomena. Flutter analyses using a standard linear unsteady aerodynamic method at this condition would raise uncertainties in the results.

This report is based on a presentation held at the AIAA Aeroelastic Prediction Workshop, Honolulu, USA, April 21-22, 2012.

Generation of unsteady aerodynamic data for transonic flutter analysis is not a trivial task due to its non-linear behaviour. Moreover, proper validation data is scarce. The AIAA Aeroelastic Prediction workshop has been organised as an attempt to provide standard validation data for transonic unsteady aerodynamics of an oscillating wing. NLR participates in the workshop with the analysis of second bending mode oscillation of the HIRENASD wing.

Description of work

To simulate the HIRENASD experiment of oscillating wing the following activities are carried out:

1. Structured multiblock grid generation of HIRENASD wing-fuselage configuration.
2. Extraction of flexibility matrix from the finite element model of HIRENASD experiment.
3. Normal modes analysis to obtain the vibration modes of HIRENASD wing.
4. Generation of fluid-structure interpolation matrix.
5. Static aeroelastic simulation for a given flow condition, i.e. not a trim analysis.
6. Simulation of HIRENASD wing oscillating in second bending mode starting from statically deformed wing obtained in step 5.

Both the mandatory and optional test cases of AIAA AePW-1 have been analyzed.

Results and conclusions

Results of simulations are compared with the available experimental data. For the static aeroelastic results good agreement with measured data is obtained in terms of steady pressure coefficients. This agreement is maintained even at the outer part of the wing implying that the aeroelastic deformation is correctly reproduced. For the simulation of second bending mode vibration, the mean pressure, the normalized magnitude of pressure and the phase angle with respect to the motion are compared with measured data. Similar to the steady pressure, the mean pressure is in good agreement with experimental data. Evenly good agreement with the measured data is also obtained for the phase angle. For the magnitude of pressure response, slightly lower response is obtained compared to the measured data. However, all features, e.g. shockwave peak, leading edge suction, etc. are reproduced properly and the general agreement is good. Comparison with other contributions during the AIAA AePW-1 workshop shows that NLR capability goes well with the state-of-the-art in transonic unsteady aerodynamic prediction.

Applicability

The method for analysing unsteady flow around oscillating configurations can be applied for preparing frequency domain aerodynamic data for flutter analysis, especially at nonlinear flow conditions.



NLR-TP-2012-476

Transonic unsteady aerodynamic analysis of HIRENASD wing oscillating in flexible modes

Contribution to AIAA Aeroelastic Prediction Workshop I,
Honolulu, USA, April 21-22, 2012

B.B. Prananta, J. van Muijden and B.J.G. Eussen

This report is based on a presentation held at the AIAA Aeroelastic Prediction Workshop, Honolulu, USA,
April 21-22, 2012.

The contents of this report may be cited on condition that full credit is given to NLR and the authors.
This publication has been refereed by the Advisory Committee AEROSPACE VEHICLES.

Customer NLR
Contract number -----
Owner NLR
Division NLR Aerospace Vehicles
Distribution Unlimited
Classification of title Unclassified
February 2013

Approved by:

Author BB Prananta 	Reviewer J van Muijden 	Managing department KMJ de Cock 
Date: 7/02/2013	Date: 07-02-2013	Date: 7-02-2013

Summary

The work presented in this report constitutes the NLR contribution to the first AIAA Aeroelastic Prediction Workshop (AePW-1). The objective of the workshop is to assess state-of-the-art methods and tools for the prediction and assessment of aeroelastic phenomena. The unavailability of a comprehensive aeroelastic benchmarking validation standard was the most important reason behind the organisation of the workshop. During the first workshop, three unsteady aerodynamic test cases are analysed. NLR's contribution focusses on the analysis of an oscillating wing tested in the High Reynolds Number Aero-Structural Dynamics (HIRENASD) experiment. Different from previous unsteady transonic aerodynamic experiments which consider rigid motions of the wing, the HIRENASD experiment focusses on the flexible modes. The unsteady aerodynamics due to second bending mode oscillation is considered at three flow conditions: low and high lift coefficient at Mach 0.80 and a condition at Mach 0.70. Prior to simulating the oscillating HIRENASD wing, static aeroelastic computations are carried out. Starting from this statically deformed shape of the wing, simulations of enforced oscillating motion due to second bending mode are carried out. Comparison of the computational results with the experimental data shows good agreement. Comparison with other computational results during the workshop confirms that the capability of ENFLOW system is parallel to the state of the art in unsteady transonic aerodynamic prediction.



This page is intentionally left blank.

Contents

1	Introduction	9
2	HIRENASD wing test case of AIAA Aeroelastic Prediction Workshop	12
2.1	HIRENASD experiment	12
2.2	CFD grid	14
2.3	Finite element model	15
2.4	Modal analysis using MSC/NASTRAN	16
3	Simulation of HIRENASD experiment	18
3.1	Method of analysis	18
3.2	Steady conditions	20
3.3	Forced oscillation of second bending mode	23
4	Conclusions	40
	References	41
	Acknowledgement	42
	Appendix A Locations of accelerometers of HIRENASD wing	43

List of Figures

<i>Figure 1</i> Illustration regarding the flutter behaviour at the extremes of the flight envelope, taken from Refs. [18][17], showing the existence of load-factor-dependent dips in the flutter speed in transonic condition and second transonic dip related to flow separation. The experiment was performed at NLR high speed tunnel in 1982.	10
<i>Figure 2</i> Overview of HIRENASD configuration tested in the European Transonic Wind tunnel used as the test case for the present study, Ref. [6][8].	13
<i>Figure 3</i> Overview of the CFD grid for the flow simulation around HIRENASD wing.	14
<i>Figure 4</i> Overview of the finite element models showing the components of the HIRENASD experimental setup. The inset shows the models in an assembled state. The light blue and orange coloured components are the model of the piezo linear stack actuators.	15
<i>Figure 5</i> Vibration modes of the HIRENASD wing based on the finite element model of the wing only, clamped at its root. The contours represent the distribution of displacements of the vibration mode.	16
<i>Figure 6</i> Overview of modified fluid structure control points, i.e. a subset of surface nodes on the finite-element model used for force and displacement transfer between aerodynamic and structural dynamic models.	17
<i>Figure 7</i> Pressure distribution of HIRENASD wing at a Mach number of 0.80, Reynolds number of 7 million and an angle-of-attack of 1.5 deg.	20
<i>Figure 8</i> Comparison of computed and measured pressure coefficients at an angle-of-attack of 1.50 deg at a flow condition corresponding to ETW132 data point of HIRENASD experiment.	21
<i>Figure 9</i> Comparison of computed and measured pressure coefficients at an angle-of-attack of -1.34 deg, representing a low lift condition, at a flow condition corresponding to ETW250 data point of HIRENASD experiment.	22
<i>Figure 10</i> Comparison of computed and measured pressure coefficients at an angle-of-attack of 1.50 deg at a flow condition corresponding to ETW155 data point of HIRENASD experiment.	23
<i>Figure 11</i> Overview of second bending mode shape mapped to the aerodynamic grid using spline method of Ref.[5], note that only data for the wing has been used. The shade represents the undeformed surface, the intersections with the deformed surface constitutes the node lines of the mode.	24
<i>Figure 12</i> Comparison of averaged pressure distribution on the HIRENASD wing between computed and measured data for ETW159 data point of HIRENASD experiment for two amplitudes of oscillation.	26
<i>Figure 13</i> Comparison of the normalised real part of unsteady pressure on the HIRENASD wing between computed and measured data for ETW159 test points of HIRENASD experiment for two amplitudes of oscillation.	27



Figure 14 Comparison of the normalised imaginary part of unsteady pressure on the HIRENASD wing between computed and measured data for ETW159 test points of HIRENASD experiment for two amplitudes of oscillation. 28

Figure 15 Comparison of the normalised magnitude of unsteady pressure on the HIRENASD wing between computed and measured data for ETW159 test points of HIRENASD experiment for two amplitudes of oscillation. 29

Figure 16 Comparison of the phase angle of the pressure with respect to the motion of the reference point on the HIRENASD wing between computed and measured data for ETW159 test point of HIRENASD experiment for two amplitudes of oscillation..... 30

Figure 17 Comparison of the average pressure on the HIRENASD wing between computed and measured data for ETW271 test points of HIRENASD experiment for two amplitudes of oscillation31

Figure 18 Comparison of the magnitude of unsteady pressure on the upper side of HIRENASD wing between computed and measured data for ETW271 test point of HIRENASD experiment for two amplitudes of oscillation. 32

Figure 19 Comparison of the magnitude of unsteady pressure on the lower side of HIRENASD wing between computed and measured data for ETW271 test point of HIRENASD experiment for two amplitudes of oscillation. 33

Figure 20 Comparison of the phase angle of unsteady pressure with respect to the motion of reference point on the HIRENASD wing between computed and measured data for ETW271 test point of HIRENASD experiment for two amplitudes of oscillation..... 34

Figure 21 Comparison of the average pressure on the HIRENASD wing between computed and measured data for the optional case of ETW155 test points of HIRENASD experiment. 35

Figure 22 Comparison of the real part of unsteady pressure on the HIRENASD wing between computed and measured data for the optional case of ETW155 test points of HIRENASD experiment..... 36

Figure 23 Comparison of the imaginary part of unsteady pressure on the HIRENASD wing between computed and measured data for the optional case of ETW155 test points of HIRENASD experiment..... 37

Figure 24 Comparison of the magnitude of unsteady pressure on the HIRENASD wing between computed and measured data for the optional case of ETW155 test points of HIRENASD experiment..... 38

Figure 25 Comparison of the phase angle of unsteady pressure with respect to the motion of reference point on the HIRENASD wing between computed and measured data for the optional case of ETW155 test points of HIRENASD experiment 39

Abbreviations

AIAA	American Institute of Aeronautics and Astronautics
AePW-1	First Aeroelastic Prediction Workshop
EARSM	Explicit Algebraic Reynolds Stress Model
ENFLOW	NLR in-house developed CFD simulation system, consists of ENDOMO domain modeller, ENGRID grid generator and ENSOLV flow solver
HIRENASD	High Reynolds Number Aero-Structural Dynamics
Re	Reynolds number
RANS	Reynolds-Averaged Navier-Stokes
TNT	Turbulent Non-Turbulent, NLR variant of k - ω turbulence model, Ref. [13].

Symbols

C_p	coefficient of pressure
E	modulus of elasticity, tensile modulus, Young's modulus
f	frequency in Hertz
$F(Q, \dot{x}; Re_\infty, M_\infty)$	fluxes of RANS equations
k - ω	two-equation turbulence model based on turbulent kinetic energy (k) and specific dissipation rate (ω)
k	reduced frequency, defined as $\omega L_{REF}/(2U_\infty)$
Q	flow state vector $Q = [\rho, \rho \bar{u}, \rho E, \rho T_1, \dots, \rho T_{NT}]^T$
q_∞	freestream dynamic pressure, $0.5 \rho_\infty U_\infty^2$
$S(Q, \dot{x}, t; Re_\infty, M_\infty)$	source term of RANS equations
\bar{u}	flow velocity vector $[u, v, w]^T$ in x , y and z -directions
$[\rho T_1, \dots, \rho T_{NT}]$	conservative turbulent variables, depends on the type of turbulence model, in present study $N_T=2$ and $[\rho T_1, \rho T_2] = [\rho k, \rho \omega]$
U_∞	freestream air velocity, flight speed
\bar{U}	speed index, defined as $U_\infty/(\omega_{REF} L_{REF} \sqrt{\mu})$
x, \dot{x}, \ddot{x}	displacement, velocity and acceleration, respectively
α	angle of attack
ϕ_i	mode shape of i -th vibration mode
μ	mass ratio of structure over air, defined as $m_{REF}/(\rho_\infty L_{REF}^3)$
ρ_∞	freestream air density
ω	circular frequency in rad/sec; specific turbulent kinetic energy dissipation rate

1 Introduction

One of the most critical tasks during the development and modification of an aircraft concerns the flutter clearance, i.e. ensuring that a catastrophic dynamic aeroelastic instability does not occur within the design flight envelope. In most cases, following the most common means of compliance to the regulation, the activities for flutter clearance culminate in a potentially dangerous flight flutter test. Reliable flutter analyses have to be carried out prior to the flight test campaign to ensure freedom from flutter and specifically to contribute to the success of the test.

Due to the nature of a flight flutter test, the flow condition imposed on the aircraft can be far off the cruise condition, i.e. at the boundary of the flight envelope. Complex flow phenomena can be expected to occur such as flow separation induced by shockwaves. Standard linear unsteady aerodynamic methods such as doublet lattice or kernel function methods can not model these phenomena. Flutter analyses using a standard linear unsteady aerodynamic method at this condition would raise uncertainties in the results.

The flutter behaviour at transonic flow can be illustrated nicely using the results of Ref. [16][17], as shown in Figure 1. An exploratory experiment was carried out at NLR at the beginning of the 80's regarding the flutter behaviour of a modern transport type wing with supercritical airfoil sections. Wing with supercritical airfoil sections is known to be sensitive to the change in the flow condition. The experiment has therefore been conducted to investigate the behaviour of flutter with respect to the static state, i.e. the angle of attack, at transonic flow condition. Figure 1 shows the experimental setup (upper right figure), the flutter diagram (upper left figure) and the state of the flow at the trailing edge at a point along the span (lower left figure). In the flutter diagram, two groups of curves are plotted, the upper group contains the lines separating the stable and unstable conditions, also called flutter boundary, and the lower group contains the frequencies of the vibration, indicating the mechanism of the flutter. The numbers along the curves represent the angles-of-attack during the test. It can be seen that the flutter boundary depends strongly on the angle of attack. Since the structural model for the wind-tunnel experiment can be considered linear, this genuinely non-linear behaviour should originate from the unsteady aerodynamic forces. This means that at this typical transonic flow condition the dynamic state of the unsteady aerodynamic force depends on its static state. This dependency to the angle-of-attack can only be modelled using non-linear aerodynamic methods. Another feature that commonly occurs at transonic flow is the tendency for a significant flutter speed reduction, known as transonic dip. Typical flutter analysis methods using linear aerodynamics miss such behaviour, see Figure 1.

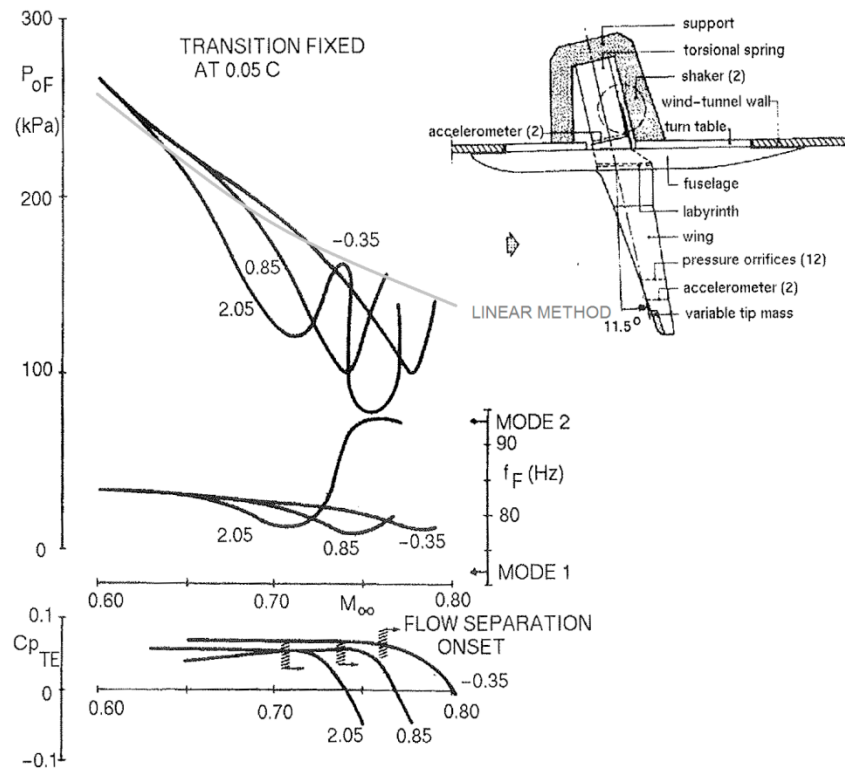


Figure 1 Illustration regarding the flutter behaviour at the extremes of the flight envelope, taken from Refs. [17][16], showing the existence of load-factor-dependent dips in the flutter speed in transonic condition and second transonic dip related to flow separation. The experiment was performed at NLR high speed tunnel in 1982.

It is clear that suitable unsteady aerodynamics methods have to be applied when analysing flutter behaviour in transonic flow. A common approach to generate unsteady aerodynamic data employs CFD methods, see e.g. Ref.[12][17]. The use of CFD, however, involves a large amount of parameters, underlying both the physical modelling and the numerical solution methods, which have to be properly considered. To gain experience and to improve confidence on using CFD for generating unsteady aerodynamic data for flutter analysis, various validation cases have been analysed. The analysed validation cases, however, mostly concern rigid motion of the configuration. A realistic flutter analysis, on the other hand, requires modelling of flexible vibration modes. It can be stated that in general, proper validation data for unsteady transonic aerodynamic cases is scarce.

Recently, several organizations proposed a common activity in validating unsteady transonic aerodynamic methods, i.e. the First AIAA Aeroelastic Prediction Workshop (AePW-1). The group identified the need to:



1. Identify errors and uncertainties in computational aeroelastic methods,
2. Identify gaps in existing aeroelastic validation databases,
3. Provide roadmap of path forward.

Towards this end, three challenging test cases are offered for analysis. This report presents the contribution of NLR in this workshop. NLR's contribution focusses on the analysis of an oscillating wing tested in the High Reynolds Number Aero-Structural Dynamics (HIRENASD) experiment. Details of the contribution will be discussed in chapter 2 and chapter 3.

2 HIRENASD wing test case of AIAA Aeroelastic Prediction Workshop

The 1st AIAA Aeroelastic Prediction Workshop (AePW-1) was sponsored by the Structural Dynamics Technical Committee of AIAA with the objectives to assess state-of-the-art computational aeroelasticity (CAe) methods as practical tools for the prediction of static and dynamic aeroelastic phenomena and responses on relevant geometries. Part of the activities concerns comparative computational studies on selected test cases. Several test cases are defined focussing on unsteady transonic flow aspects. The AePW-1 test cases are:

1. Rectangular supercritical Wing (RSW), see Ref. [2].
2. Benchmark Supercritical Wing (BSCW), see Ref. [3].
3. HIRENASD wing, see Refs. [6][8].

The geometry and measurement data for these test cases are made available by the organising committee of AePW-1.

In the present study, the HIRENASD test case is selected due to its uniqueness in the type of motion. The measurement data is obtained on a wing oscillating in flexible modes. The other two experiments concern rigid oscillation of the wing.

2.1 HIRENASD experiment

From the available measurement data, the experiment of the High Reynolds Number Aero-Structural Dynamics (HIRENASD) project is of particular interest, Ref.[6][8]. The experiment was carried out at the cryogenic European Transonic Wind-Tunnel, i.e. at Reynolds numbers relevant to real flight and it is targeted specifically for generating validation data for computational aeroelastic simulation methods.

The HIRENASD project was funded by the German Research Foundation (DFG) through the Collaborative Research Centre “Flow Modulation and Fluid-Structure Interaction at Airplane Wings” (SFB 401). The objectives of the project were twofold:

1. To gain a better aero-structural dynamics understanding and knowledge in the transonic regime up to real flight Reynolds numbers, and
2. To obtain experimental data in a wide range of Reynolds numbers and aerodynamic loads for current and future aerodynamic and aeroelastic research.

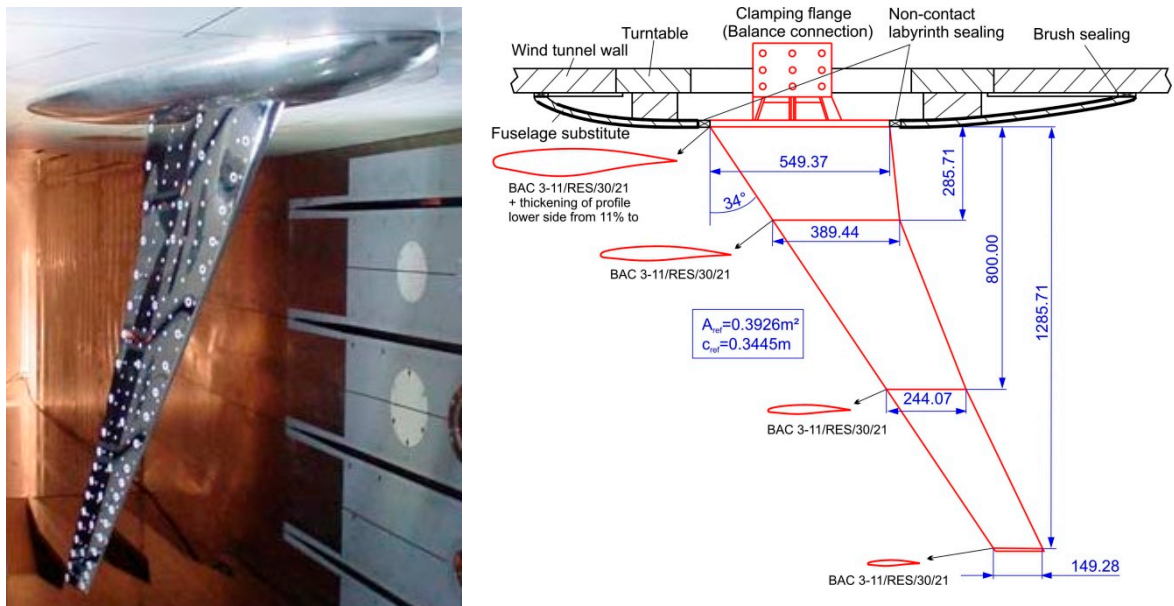


Figure 2 Overview of HIRENASD configuration tested in the European Transonic Wind tunnel used as the test case for the present study, Ref. [6][8].

The tested wing-body configuration, without tail, is depicted in Figure 2. It is a half model of a typical large civil transport aircraft wing with moderate sweep angle. The wing has a supercritical aerofoil called the BAC aerofoil, Ref. [10]. The model hangs on the ceiling of the tunnel so that gravity has a negligible effect on the deformation.

The model setup of the HIRENASD experiment is directed towards an unsteady dynamic experiment. An excitation system is built at the root of the wing to bring the wing into a forced oscillation. By exciting the wing at the coupled (fluid-structure) natural frequencies the motion is assumed to be dominated by the associated mode shape. In this sense this experiment produces a unique set of unsteady aerodynamic data of a wing oscillating in its flexible modes. To the author's knowledge, so far, all other unsteady aerodynamic experiments are intended to excite the model with rigid motion, i.e. rigid pitching or heaving.

For the present study, various measurement data are used, including test points 132, 250, 159 and 271, see Ref. [6]. The HIRENASD measurements concern conditions with a Mach number between 0.70 to 0.88, Reynolds number between 7 and 50 millions, and ratio of dynamic pressure over the Young modulus between 0.22×10^{-6} and 0.70×10^{-6} . The specific conditions used for the AIAA AePW-1 workshop will be given in detail in the next chapter. Note that due to the cryogenic conditions used during the experiment, the Young modulus of the material used for the wind-tunnel model will be different from one test condition to another test condition. To allow the use of a single finite element model with a temperature-independent definition of the

Young modulus, the dynamic pressure for static aeroelastic analyses should be derived from the value of the ratio of dynamic pressure over the Young modulus, q/E .

2.2 CFD grid

The available grids for aerodynamic simulation based on structured multiblock methods are not fully suitable for NLR's in-house CFD method ENFLOW. Therefore a new computational grid has been generated. The grid generation has been started from the block topology available on the repository of AePW-1, generated by ICEM GmbH. The necessary modifications can be summarised as follow:

- The blocks are subdivided for improved parallelisation runs on NLR computer, the number of blocks becomes 352.
- To improve the boundary layer resolution (one Navier-Stokes wall normal direction per block only), the block arrangement close to the wing body junction is modified.
- The block dimensions are set to be suitable for automatic coarsening required for application of multigrid acceleration in the flow solver. The number of computational cells is now 9,632,768 cells with a possibility to have 4 multigrid levels.

The resulting grid has been uploaded to the AePW-1 repository for sharing with other analysts.

An overview of the NLR HIRENASD grid is shown in *Figure 3*. The figure shows the block arrangement, the surface grid and part of the symmetry plane.

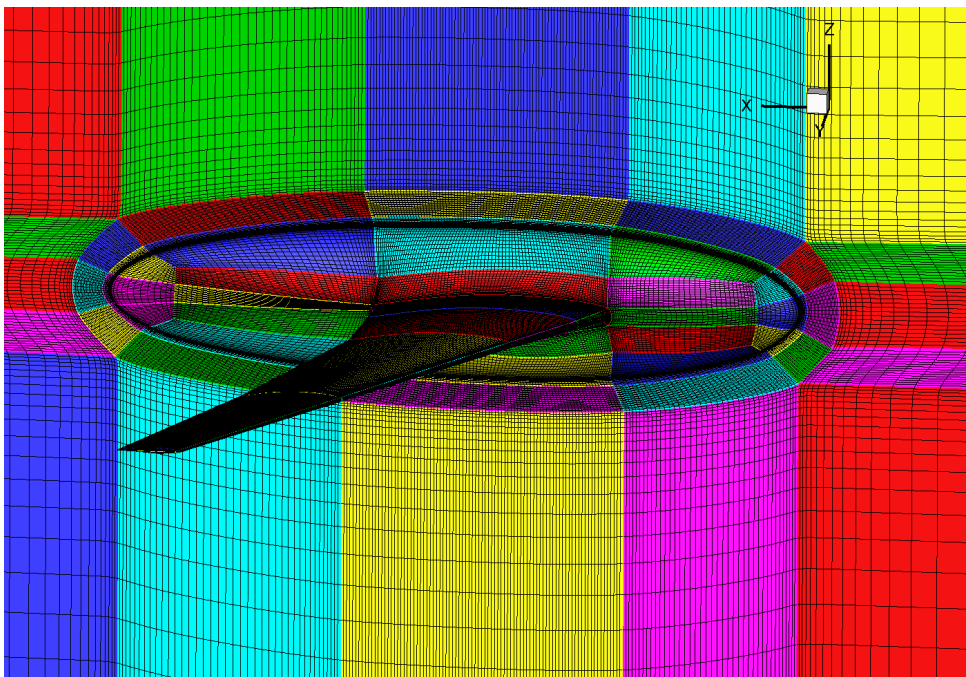


Figure 3 Overview of the CFD grid for the flow simulation around HIRENASD wing.

As can be observed in *Figure 3* the grid is clustered near wing leading edge and trailing edge.. The inclusion of the fuselage into the computational model is primarily meant for having correct interference effects since the fuselage does not move. A preliminary grid convergence study is carried out which confirms that the grid density should be good enough for the present study. The CFD grid adopts an OH topology which is suitable for grid deformation.

2.3 Finite element model

There are several finite element models of the HIRENASD wing available in Ref. [7] and Ref. [8]. Two versions of the wing model are available, one version is based on tetrahedral elements and another version is based on the hexahedral elements. During the experiment, the wing is excited using a complex actuation system based on piezo-electric linear stack actuators. Some parts of the system are subjected to low cryogenic temperature of the tunnel and other parts are protected and heated. So there are uncertainties in the precise boundary condition at the wing root. Therefore a complete model is developed as shown in *Figure 4*. In the present study, computations of normal modes have been carried out for both the wing only model with a clamping boundary condition at the root and for the full assembly model. For the wing only model, to be consistent with the full assembly model, the version using tetrahedral elements is used. The results, however, are not significantly different, especially for mode 2 and mode 5 involved in the present study. Subsequently, it is therefore decided to use the wing only model for simplicity.

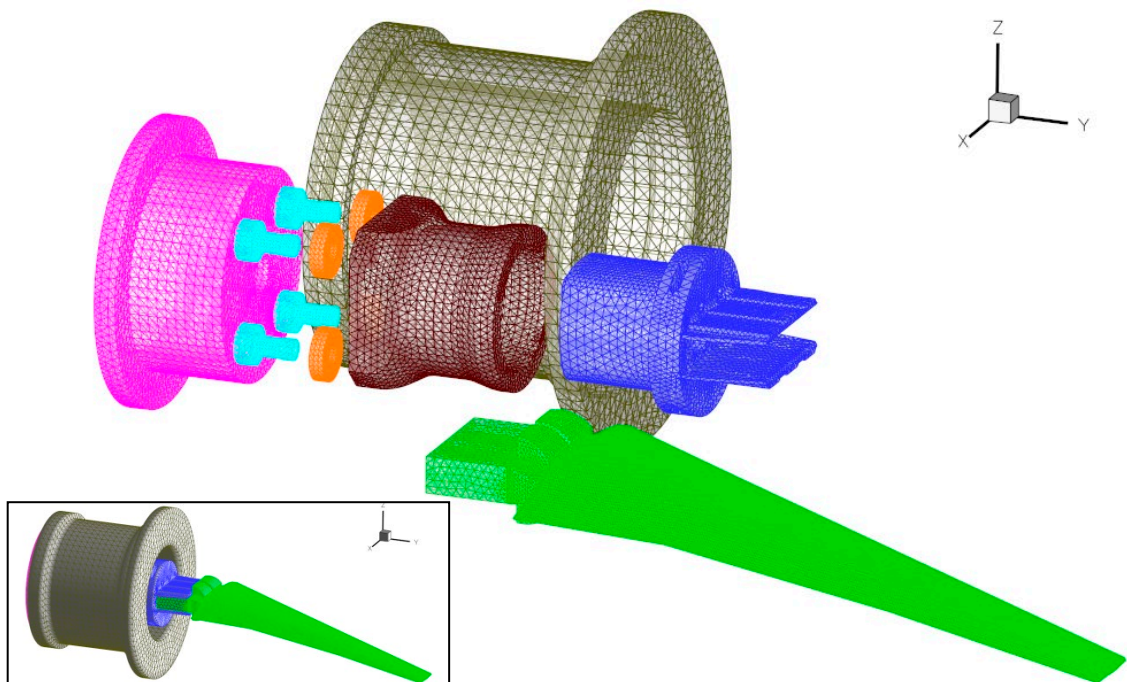


Figure 4 Overview of the finite element models showing the components of the HIRENASD experimental setup. The inset shows the models in an assembled state. The light blue and orange coloured components are the model of the piezo linear stack actuators.

2.4 Modal analysis using MSC/NASTRAN

For carrying out aeroelastic simulations in the present study, several types of structural data are required, i.e. the flexibility matrix for a static aeroelastic simulation, the mode shape data for a simulation of forced excitation and other modal data for fully coupled aeroelastic simulations.

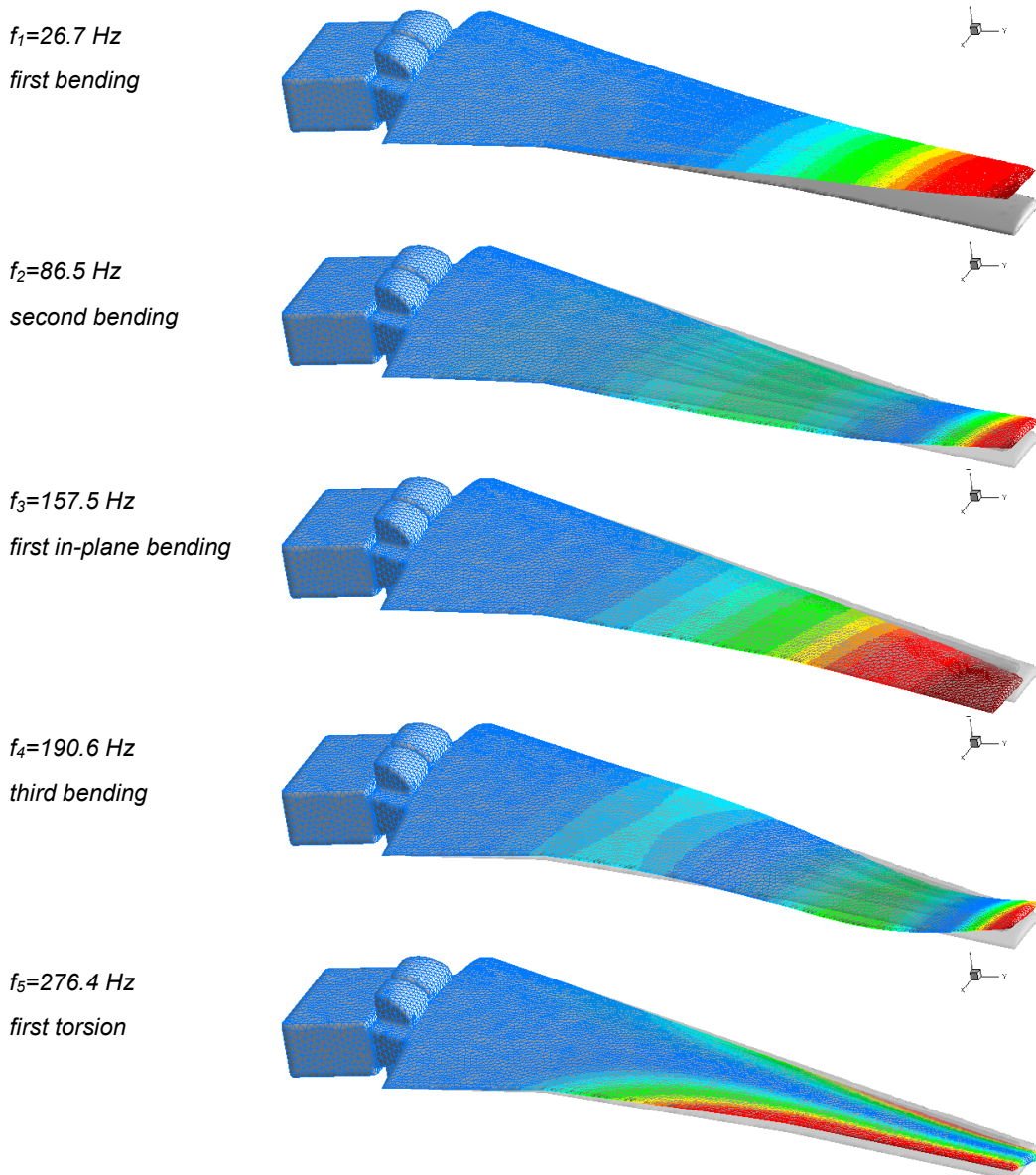


Figure 5 Vibration modes of the HIRENASD wing based on the finite element model of the wing only, clamped at its root. The contours represent the distribution of displacements of the vibration mode.

The modal data are generated using module SEMODES (SOL103) of MSC/NASTRAN, Ref. [1], based on the wing-only model with tetrahedral solid elements. An overview of the first five flexible vibration modes of the HIRENASD wind-tunnel model is shown in Figure 5. The

natural frequencies of these vibration modes are about 10 times higher than those of a real aircraft structure.

To generate the flexibility matrix, a subset of nodes on the surface is selected to represent the fluid-structure interface. For this purpose, the AePW-1 suggests to use 144 nodes on the upper surface of the HIRENASD wing. This set of nodes, however, is not suitable for the fluid-structure interpolation method applied by NLR which is based on the volume spline method, Ref.[5]. Therefore a modified set of nodes is used here. Overview of the surface nodes used as fluid-structure interface is shown in Figure 6. Unit loads in three translational directions are then defined at these fluid-structure interface nodes. The MSC/NASTRAN module SESTATIC (SOL101) is employed to compute the deformation due to these unit loads. The deformation distribution for a unit load represents a column in the flexibility matrix.

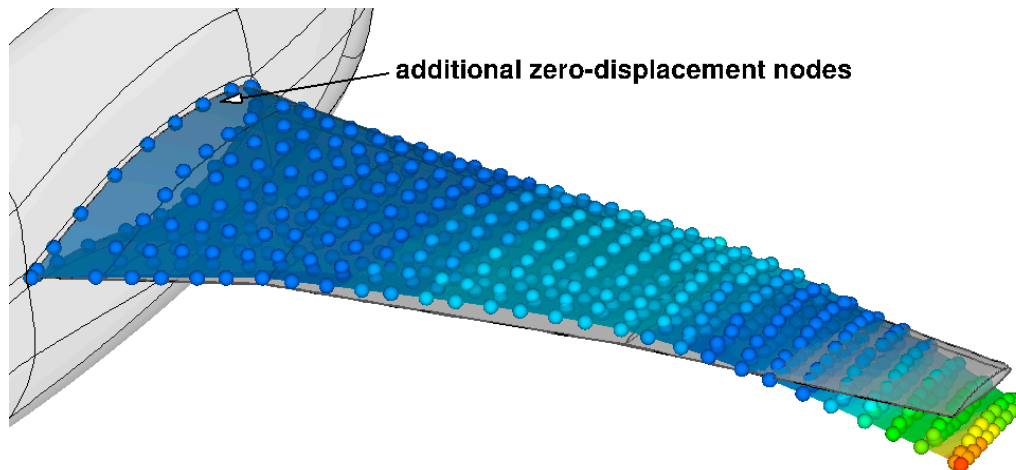


Figure 6 Overview of modified fluid structure control points, i.e. a subset of surface nodes on the finite-element model used for force and displacement transfer between aerodynamic and structural dynamic models.

3 Simulation of HIRENASD experiment

Several HIRENASD measurement conditions are selected in the AIAA AePW-1. A summary of the test cases is presented in Table 1. Case 1 and 2 at Mach 0.80 are the mandatory cases, while case 3 at a lower Mach number of 0.70 is optional. In the present work, both mandatory and optional cases have been analysed.

Table 1 Summary of AIAA AePW-1 test cases

case	Mach	Re_{MAC} [10^6]	q/E [10^{-6}]	α [deg]	k	remarks, corresponding test point, see Refs. [6][7][8][9]
1	0.80	7.0	0.22	1.50		ETW132
	0.80	7.0	0.22	1.50	0.67	ETW159
2	0.80	23.5	0.48	-1.34		ETW250
	0.80	23.5	0.48	-1.34	0.79	ETW271
3	0.70	7.0	0.22	1.50		ETW129
	0.70	7.0	0.22	1.50	0.76	ETW155

3.1 Method of analysis

The aeroelastic simulation system employed in the present study is the NLR ENFLOW system, consisting of the ENDOMO domain modeller, the ENGRID grid generator and the ENSOLV flow solver. The flow model employs the Reynolds-Averaged Navier-Stokes equations while the geometry modelling uses structured multiblock grids. The ENFLOW system has been widely applied for activities requiring high fidelity flow simulations such as aerodynamic performance prediction, aircraft-engine integration, support for wind tunnel measurement, unsteady cavity flow, unsteady flow about oscillating wing, internal flow inside aircraft cabin, etc. Applications for aeroelastic simulation can be found in Refs. [4][11][15].

The governing equations for an aeroelastic system consist of the equations governing the dynamics of the structure of the aircraft and the equations governing the flow field around the aircraft. The deformation of the structure is assumed to be relatively small, allowing the use of a linearised structural model. The nonlinear RANS equations are used to model the flow field around the aircraft. In a non-dimensional form the set of governing equations can be written as:

$$M\ddot{x} + C\dot{x} + Kx = \frac{\bar{U}^2}{2} C_A(Q, x, \dot{x}, \ddot{x}, t) + P(t) \quad (1)$$

$$\frac{\partial Q}{\partial t} + \vec{\nabla} \cdot F(Q, \dot{x}; Re_\infty, M_\infty) = S(Q, \dot{x}, t; Re_\infty, M_\infty) \quad (2)$$

These equations are coupled through the kinematic condition at the fluid/structure interface. In Equations (1) and (2), M is the mass matrix, C is the damping matrix, K is the stiffness matrix

and C_A is the aerodynamic force coefficient vector which is a function of the flow state vector $Q = [\rho, \rho \bar{u}, \rho E, \rho T_1, \dots, \rho T_{NT}]^T$ where ρ is the density, $\bar{u} = [u, v, w]^T$ is the velocity vector, E is the total energy per unit mass, and T_1, \dots, T_{NT} are the variables for the turbulence models. F and S are the flux matrix and the source term in the Euler/Navier-Stokes equations, respectively. In addition to the usual similarity parameters, i.e. the Reynolds number Re_∞ , the Mach number M_∞ , and the coefficient of aerodynamic force C_A , a fluid/structure interaction parameter, the so-called speed index \bar{U} , is involved in the governing equations. \bar{U} is defined as $U_\infty / (\omega_{REF} L_{REF} \sqrt{\mu})$, where μ is known as the mass ratio between the structure and the air surrounding the structure. All similarity parameters are invariant across the fluid/structure interface.

The Euler/Reynolds-Averaged Navier-Stokes equations are discretised following a cell-centred finite-volume method in multiblock structured grids. Second-order and fourth-order schemes are available to discretise the equations in space. The latter, however, needs reasonably smooth grids. Time-accurate integration is carried out using a dual-time stepping scheme employing the Runge-Kutta method for the relaxation in the pseudo time. Convergence acceleration is provided by the full approximation storage (FAS) multigrid method and a line relaxation method in the boundary layer regions.

In the present work, all viscous computations have been carried out using the NLR TNT (turbulent-non-turbulent) $k-\omega$ turbulence model. The TNT variant of the $k-\omega$ turbulence model, described in Ref. [13], removes the unnecessary dependency of the results on the free-stream turbulence level. Further, to handle the strong shockwave, the explicit algebraic Reynolds stress model (EARSM) is also added, see Ref. [18] for more detailed description. It is generally known that turbulence models which are formulated based on the Bradshaw assumption, Ref. [19], are more successful for computation of boundary layers under strong adverse pressure gradient, e.g. Johnson-King, Ref. [21], and Menter SST models, Ref. [20]. For cases with strong shockwaves it is also desired to apply a modified version of the explicit algebraic Reynolds stress model, which moderates the increase of the shear stress in case of a strong adverse pressure gradient. However, due to lack of experience with this new modification of the EARSM model, only the standard EARSM model is used throughout the study.

During an aeroelastic simulation, the multiblock grids have to deform to follow the deformation of the fluid/structure interface due to the aerodynamic and inertial loads. In the present work, a robust and efficient grid deformation technique has been developed. The method combines a three-dimensional spline technique, e.g. the volume spline of Ref. [8], and a standard transfinite interpolation technique. The first is applied to the block boundaries while the second is applied to the grid inside the block. A more detailed description can be found in Ref. [14].

3.2 Steady conditions

Static aeroelastic simulations are carried out at the selected test cases. The input for the simulations are the CFD grid as shown in *Figure 3* and the flexibility matrix generated at the modified fluid-structure interface nodes as depicted in *Figure 6*. *Figure 7* presents the overview of the flow around the HIRENASD configuration at a condition corresponding to case 1 of *Table 1*. One static aeroelastic simulation costs about 2 hours of wall-clock time (58 CPU hours) on four nodes of an SGI Altix computer with eight CPU cores of an Intel Xeon Nehalem processor in each node. A standard procedure is followed by first carrying out 500 multigrid iterations for rigid configuration followed by 750 multigrid iterations without aeroelastic coupling. Four grid levels are employed for multigrid acceleration.

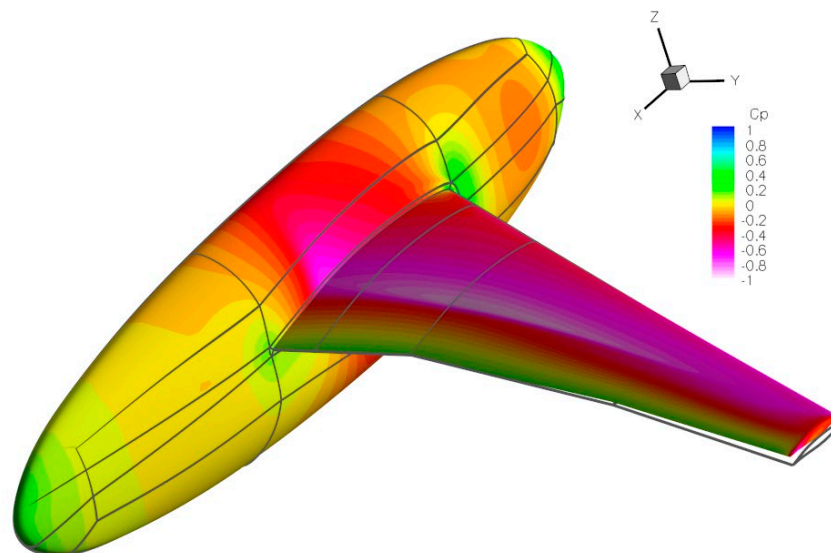


Figure 7 Pressure distribution of HIRENASD wing at a Mach number of 0.80, Reynolds number of 7 million and an angle-of-attack of 1.5 deg.

Comparison of the surface pressure coefficient at the measurement span stations between computational results and experimental data is shown in *Figure 8*. In general the agreement is good, especially for the outer region of the wing. At the inner part of the wing, the region where a strong shockwave-boundary layer interaction occurs, the predicted shockwave location seems to be slightly too aft. The good agreement at the outer part of the wing suggests that the effect of structural deformation in producing nose down twist at the outer part of the wing is correctly reproduced.

The results for case 2 of *Table 1*, i.e. the low C_L case at Mach 0.80, Reynolds number 23.5 million and angle of attack -1.34 deg. are shown in *Figure 9*. Evenly good agreement is obtained for pressure coefficient between computed and measured data. The effect of structural deformation should be small due to the low C_L condition.

Finally comparison of pressure coefficients at several span stations for the low Mach number case, i.e. case 3 of Table 1 are shown in Figure 10. Overall good agreement is obtained also at the inner wing region.

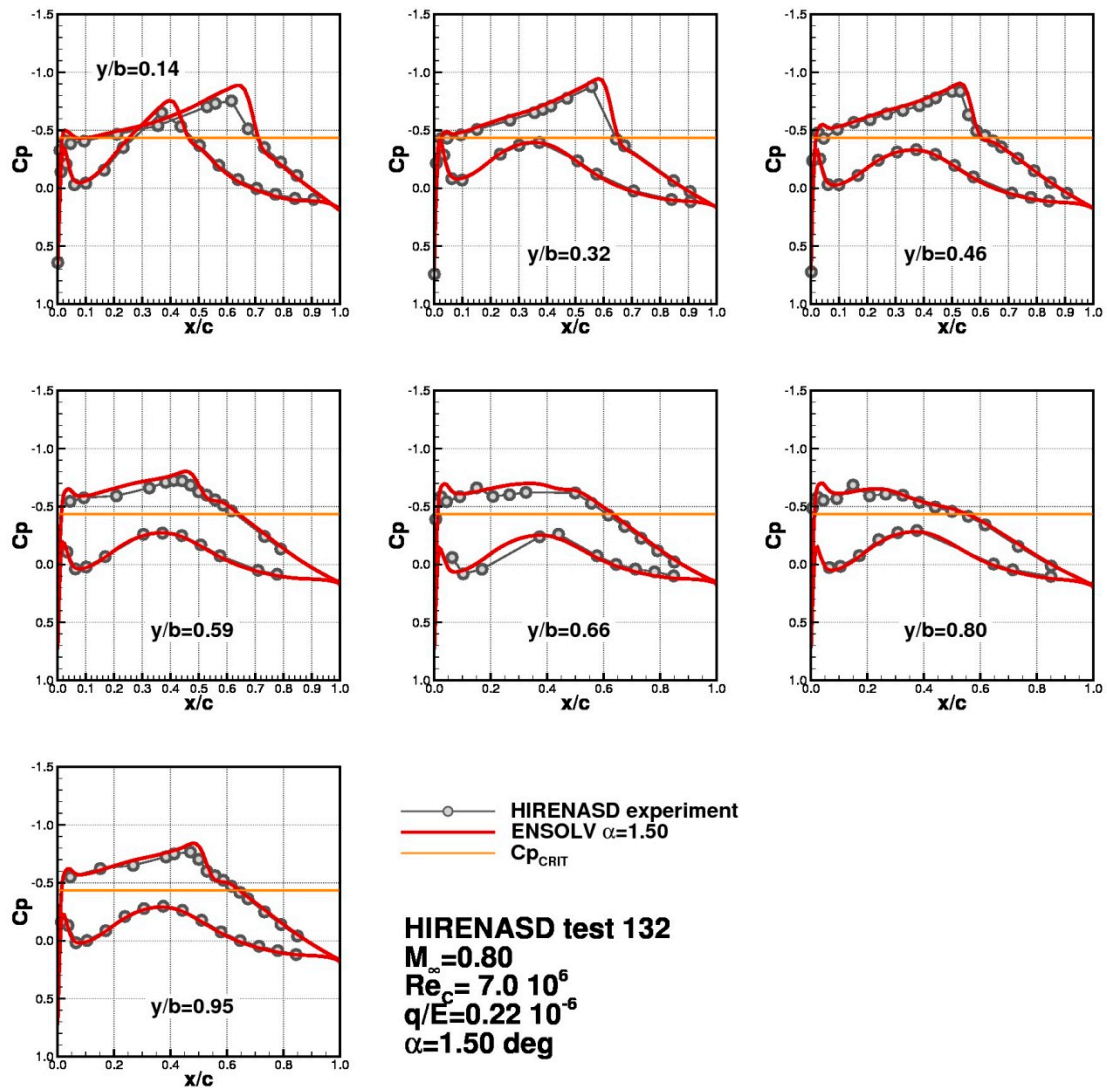


Figure 8 Comparison of computed and measured pressure coefficients at an angle-of-attack of 1.50 deg at a flow condition corresponding to ETW132 data point of HIRENASD experiment.

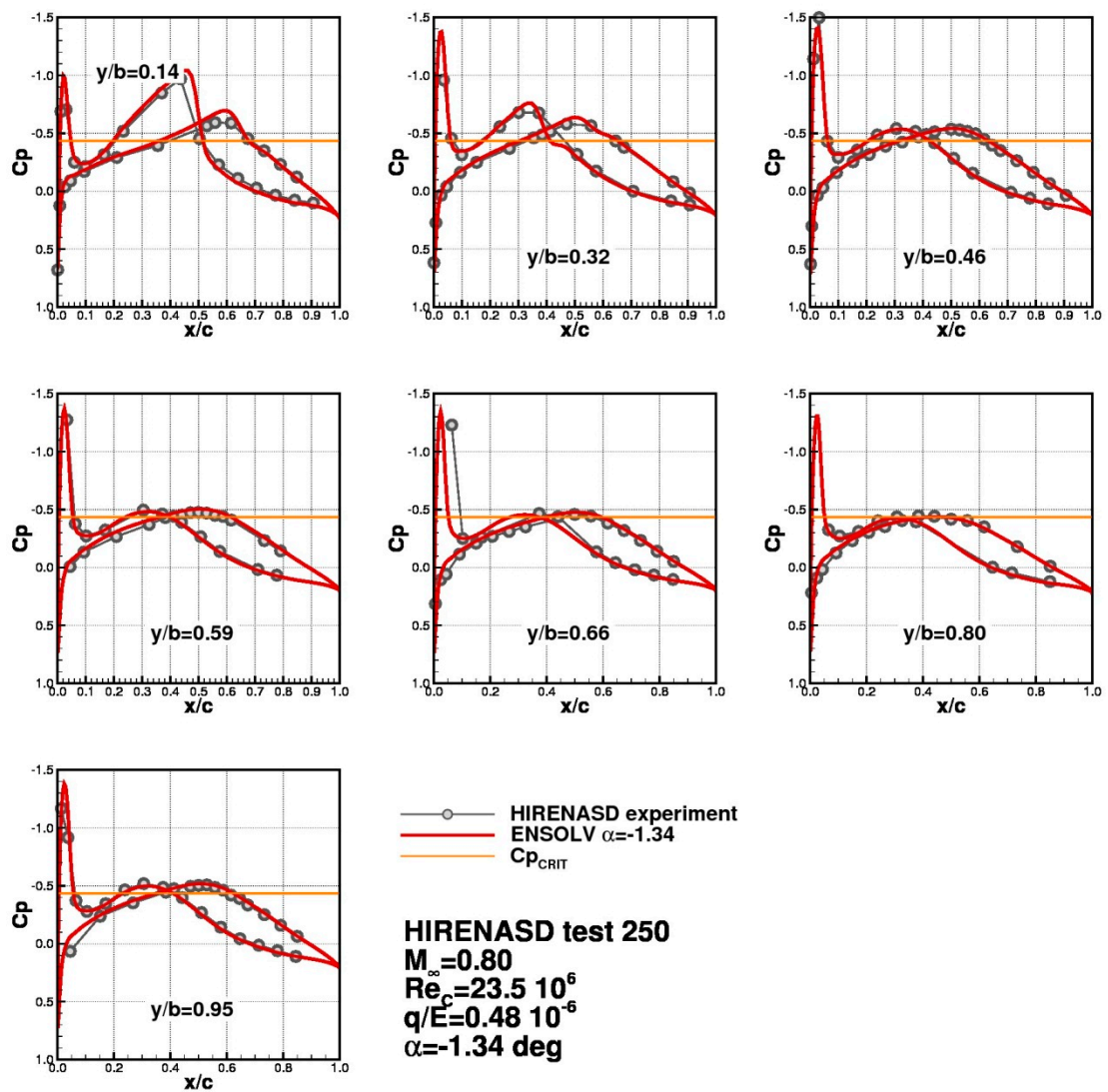


Figure 9 Comparison of computed and measured pressure coefficients at an angle-of-attack of -1.34 deg, representing a low lift condition, at a flow condition corresponding to ETW250 data point of HIRENASD experiment.

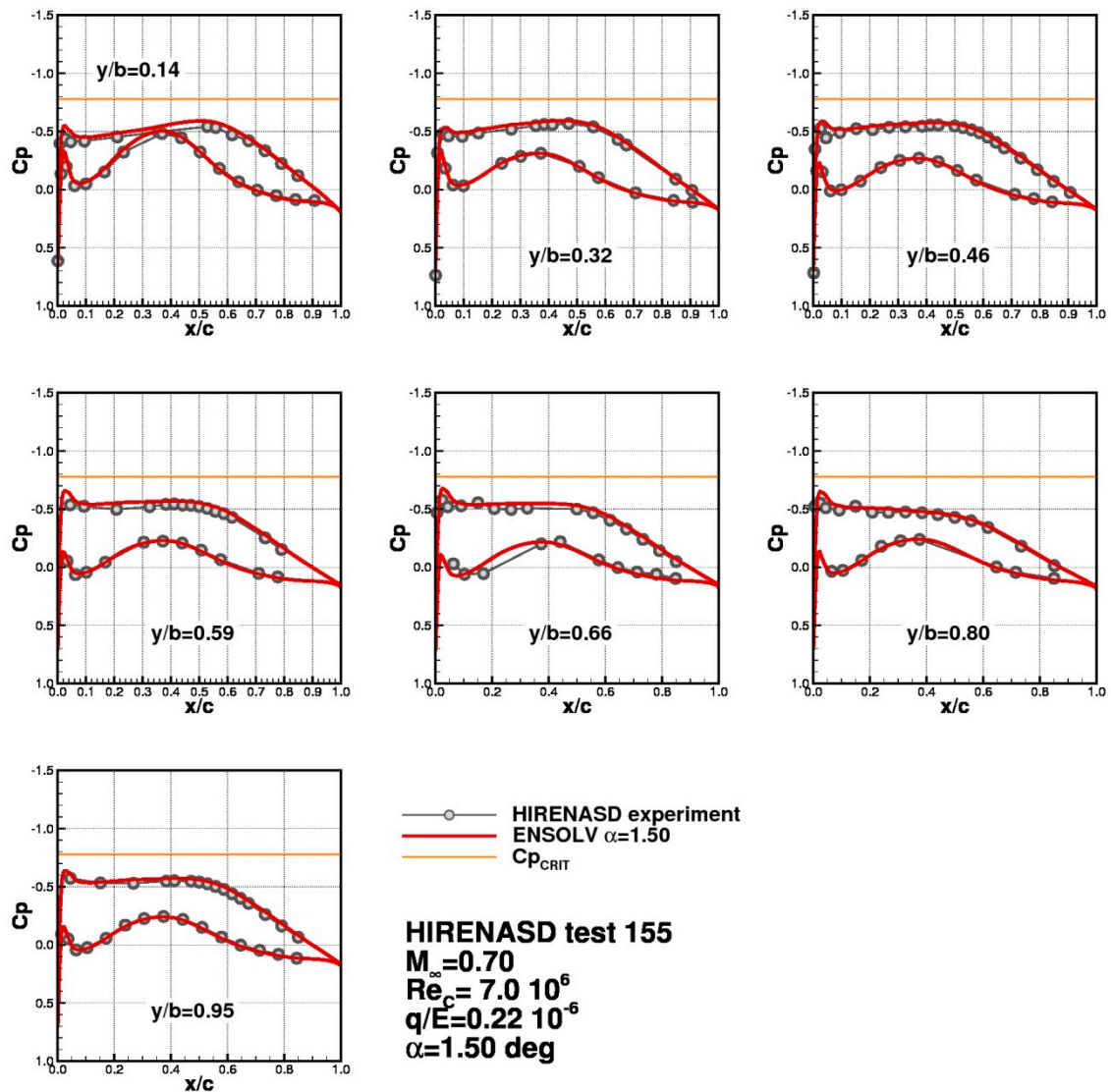


Figure 10 Comparison of computed and measured pressure coefficients at an angle-of-attack of 1.50 deg at a flow condition corresponding to ETW155 data point of HIRENASD experiment.

3.3 Forced oscillation of second bending mode

The results of dynamic simulations are now presented. The results of the HIRENASD experiment including excitation at a frequency close to the second bending mode are reproduced using forced motion simulation with second bending mode. This approach is justified because the experimental flow condition is far below the flutter speed which means that the fluid-structure coupling is relatively weak. The weak fluid-structure coupling implies that the motion can be considered synchronous, i.e. without phase differences between locations in the wing. Therefore, instead of using complex vibration mode, real vibration mode computed at wind-off condition is used in this exercise.

To enable the analysis, the second bending mode computed on the structural model has to be mapped to the aerodynamic model. Figure 11 depicts the mapped mode shape on the aerodynamic grid from the structural data. Two node lines are observed which are typical for a 2nd bending mode.

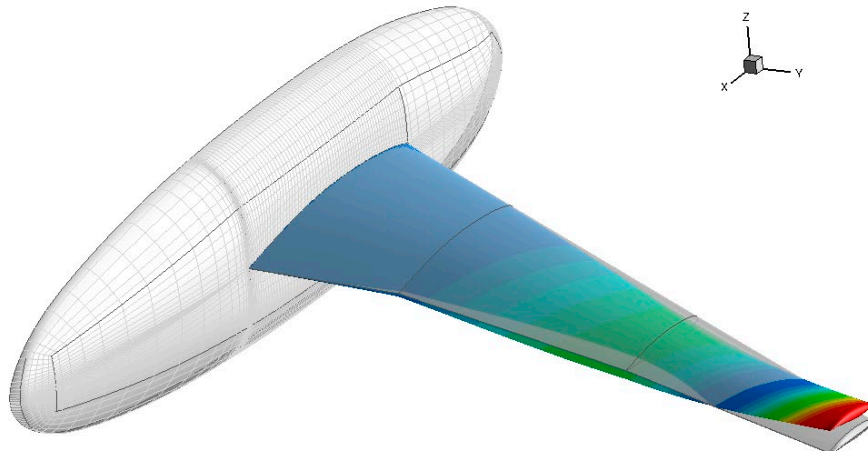


Figure 11 Overview of second bending mode shape mapped to the aerodynamic grid using spline method of Ref.[5], note that only data for the wing has been used. The shade represents the undeformed surface, the intersections with the deformed surface constitutes the node lines of the mode.

For a forced vibration analysis the inputs for the simulations are: the vibration mode, the frequency and the amplitude of the oscillation. The procedure to carry out the analysis consists of two steps:

1. The first step is a static aeroelastic simulation starting from a jig shape to obtain the statically loaded condition, see section 3.2.
2. The second step is a sinusoidal motion about the statically loaded configuration due to the second bending mode. The state of the aerodynamic surface at a certain time is:

$$\vec{x}(t) = \vec{x}_{JIG} + \Delta\vec{x}_{STATIC} + q_{AMP} e^{ikt} \vec{\phi}_2 \quad (3)$$

3. The third step is a post-processing of the pressure data using a Fourier decomposition based on the excitation frequency. The unsteady pressure data is normalised with respect to the deformation at accelerometer number 15/1 of the HIRENASD wing, see also Figure A.1.

Simulations for four periods of oscillation are carried out to ensure that a periodic solution is obtained. In each period 32 time steps are used with 60 multigrid cycles of sub-iteration. This parameter setting is very conservative. The wall clock time for one unsteady run is about 11.5 hours on four nodes of an SGI Altix computer with 8 CPU cores of Intel Xeon Nehalem processor in each node. The total CPU time is 364 hours.

The results of the case 1 are presented in Figure 12, Figure 13 and Figure 14 in terms of the averaged pressure, the normalised real part of pressure and the imaginary part of the pressure, respectively. The normalisation is computed with respect to the amplitude of displacement at the reference point. The reference point is the earlier-mentioned location of the accelerometer 15/1 in Figure A.1. The real part of the pressure contributes to the aerodynamic forces which are in the same phase as the structural motion, while the imaginary part of the pressure contributes to the aerodynamic damping, i.e. 90 degree phase lag with respect to the motion. To adhere the standard data for the AIAA AePW-1 workshop, the results are also presented as the normalised magnitude of pressure and the phase angle of the pressure with respect to the reference point. These data are shown in Figure 15 and Figure 16, respectively.

To investigate the linearity of the case, two simulations have been carried out with different amplitudes. The first amplitude is the mandatory value of the AIAA AePW-1 workshop, while the second amplitude is twice as large. Figure 12 shows that the effects of the amplitude to the averaged pressure are small. Similar to the steady case, good agreement is obtained between computational results and experimental data. The good agreement in terms of real and imaginary parts of the pressure also suggests that the aerodynamic damping is predicted satisfactorily. A slightly more significant effect of amplitude on the unsteady part of the pressure is observed; see Figure 13, Figure 14 and Figure 15. Although understandably the amplitude will mostly influence the pressure peak due to shockwave travel, pressure in front of the shockwave is also slightly changed. In general, the agreement with the experiment is good. Regarding the phase angle between the pressure signal and the deformation of reference point, good agreement with the experimental data is obtained.

For case 2, shown in Figure 17, Figure 18, Figure 19 and Figure 20, similar conclusions can be drawn for the averaged pressure, the magnitude of the pressure and the phase angle. Due to the low C_L condition, the pressure level at the upper and lower side is almost similar. Therefore separate plots are made, Figure 18 for the lower side and Figure 19 for the upper side. It can be seen that all features of the pressure distribution are properly reproduced. However, the level of pressure is slightly lower compared to the experimental data.

Finally, the results for the optional case at a lower Mach number of 0.70 are shown in Figure 21, Figure 22, Figure 23, Figure 24 and Figure 25 for the averaged pressure, the normalised real and imaginary parts of the pressure, the normalised magnitude of pressure and the phase angle of pressure with respect to the reference point, respectively. Only one amplitude of oscillation has been considered since nonlinearity with respect to amplitude is not expected for this case. Very good agreement with the experimental data is obtained.

It may be concluded that the cases considered in AIAA AePW-1, the NLR ENFLOW system performs well in predicting transonic unsteady aerodynamic forces for oscillating wing. Moreover, amplitude study shows that the unsteady pressure can be considered a small perturbation with respect to the steady pressure.

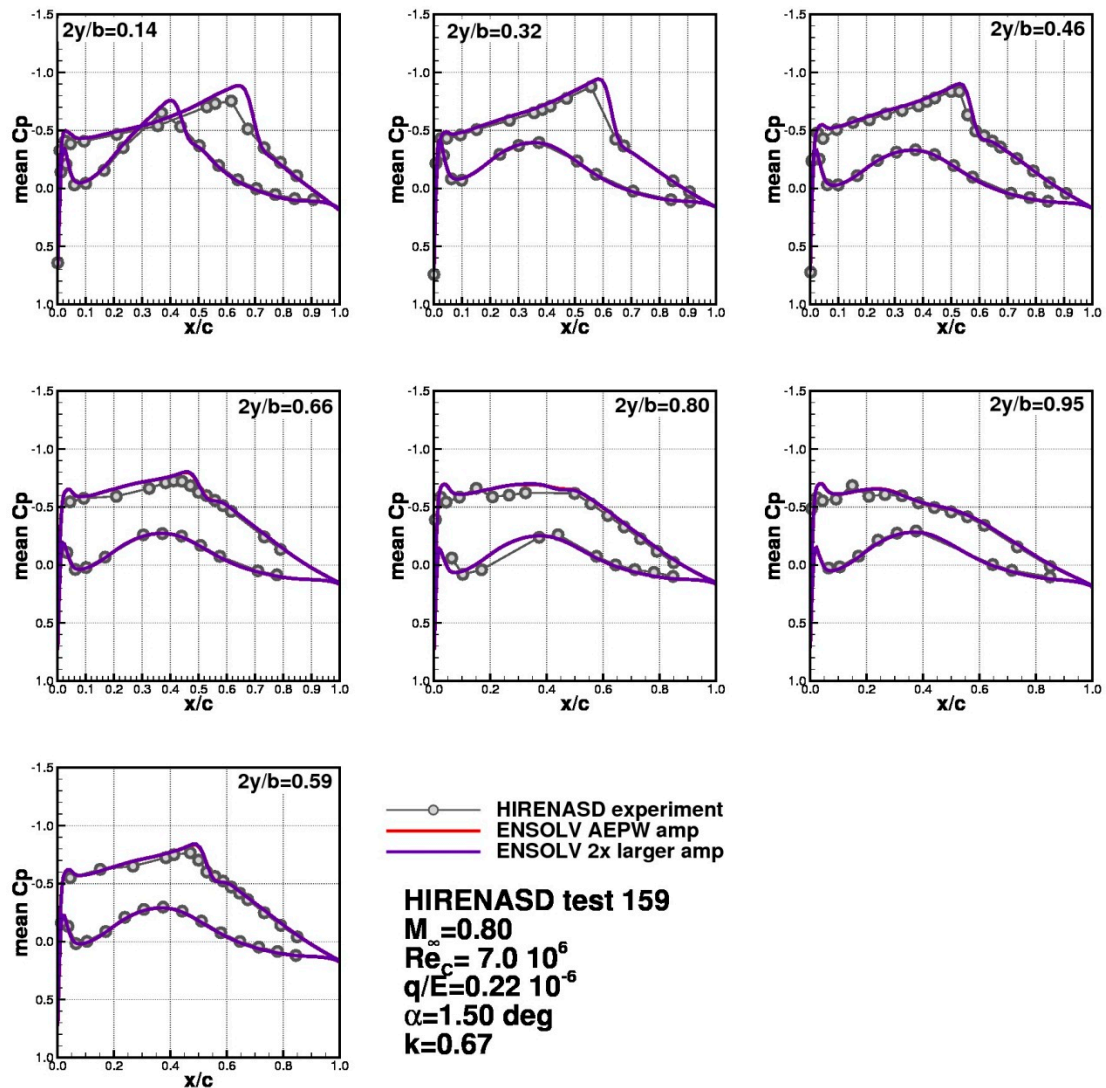


Figure 12 Comparison of averaged pressure distribution on the HIRENASD wing between computed and measured data for ETW159 data point of HIRENASD experiment for two amplitudes of oscillation.

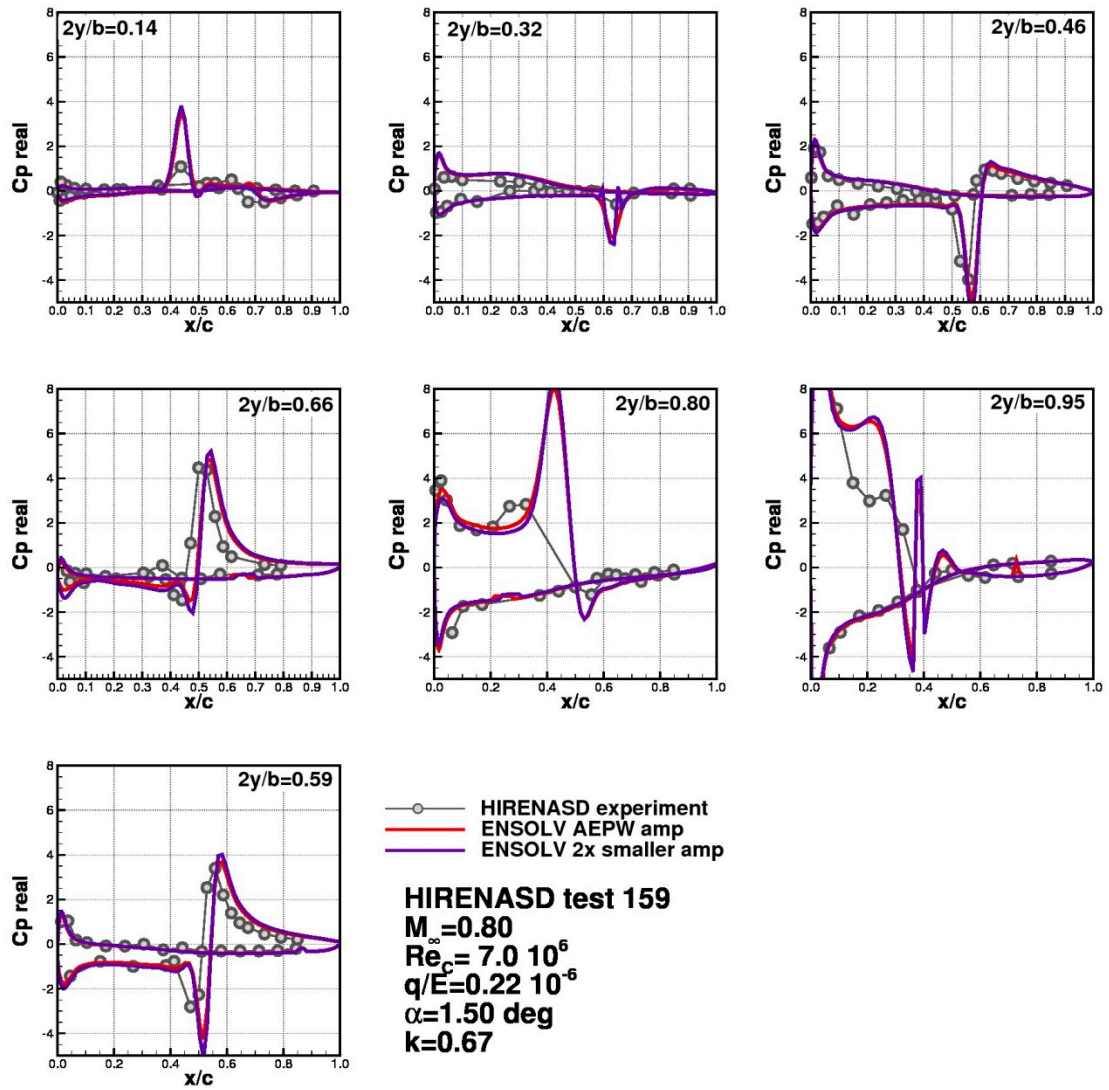


Figure 13 Comparison of the normalised real part of unsteady pressure on the HIRENASD wing between computed and measured data for ETW159 test points of HIRENASD experiment for two amplitudes of oscillation.

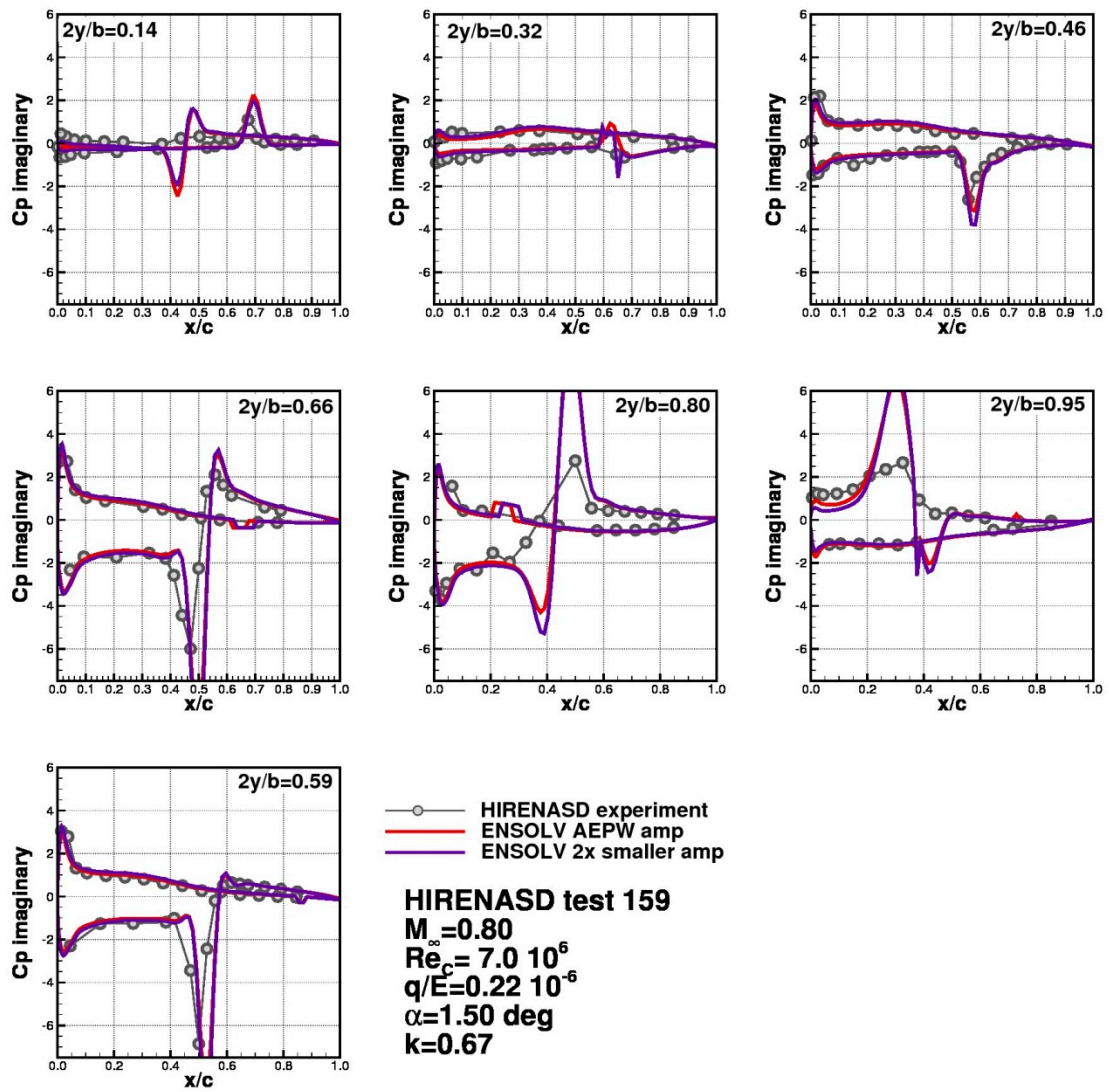


Figure 14 Comparison of the normalised imaginary part of unsteady pressure on the HIRENASD wing between computed and measured data for ETW159 test points of HIRENASD experiment for two amplitudes of oscillation.

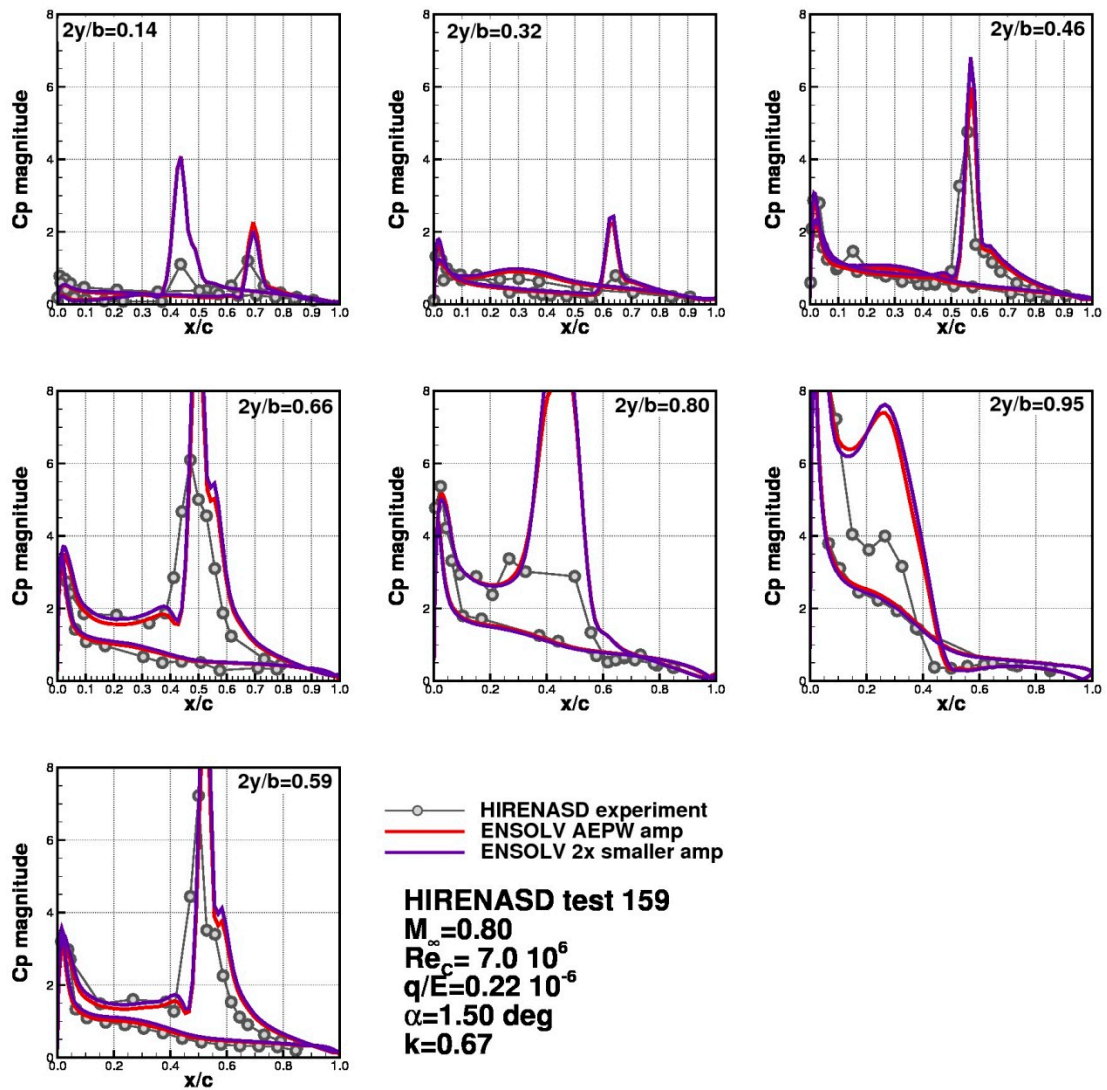


Figure 15 Comparison of the normalised magnitude of unsteady pressure on the HIRENASD wing between computed and measured data for ETW159 test points of HIRENASD experiment for two amplitudes of oscillation.

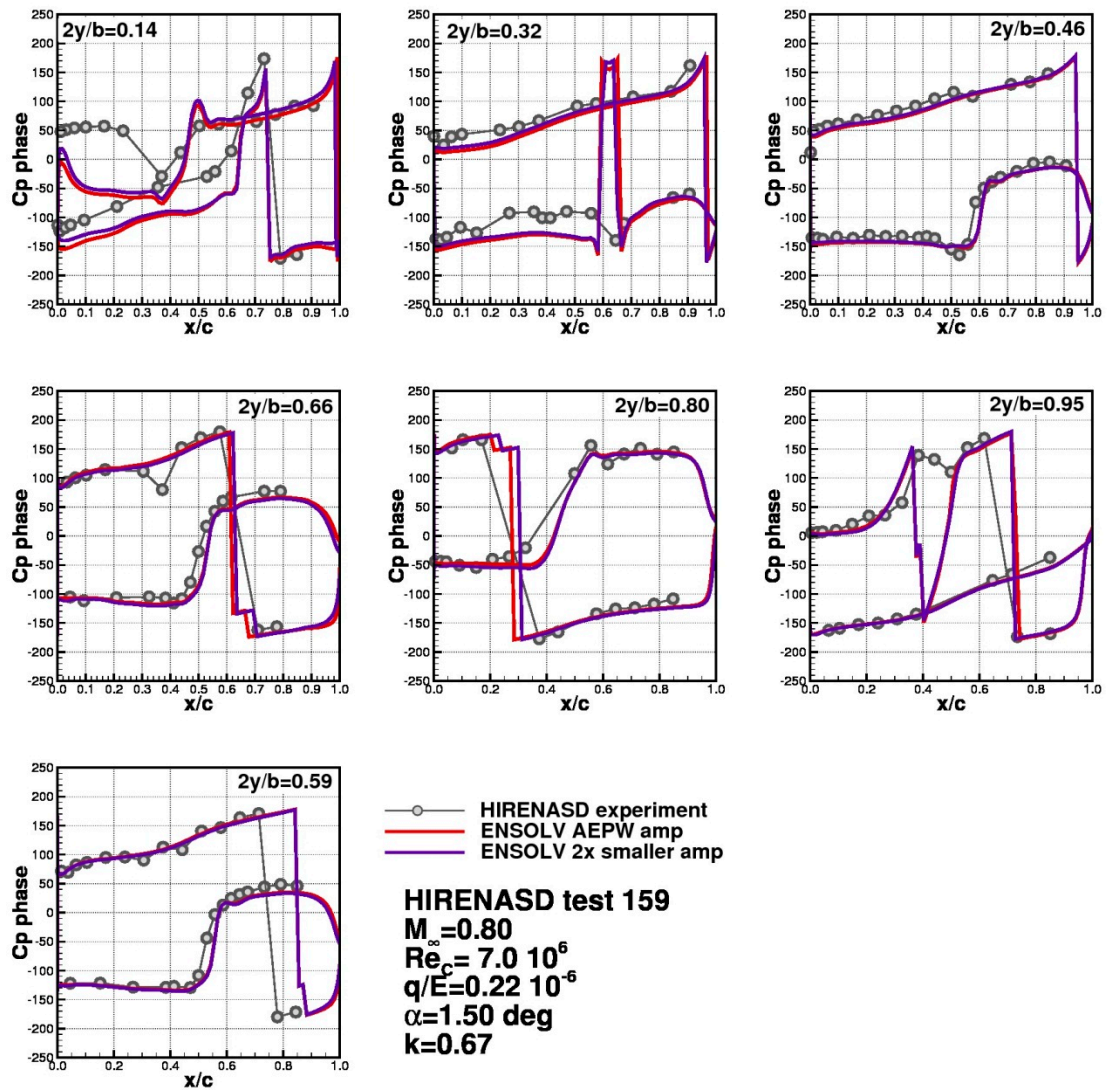


Figure 16 Comparison of the phase angle of the pressure with respect to the motion of the reference point on the HIRENASD wing between computed and measured data for ETW159 test point of HIRENASD experiment for two amplitudes of oscillation.

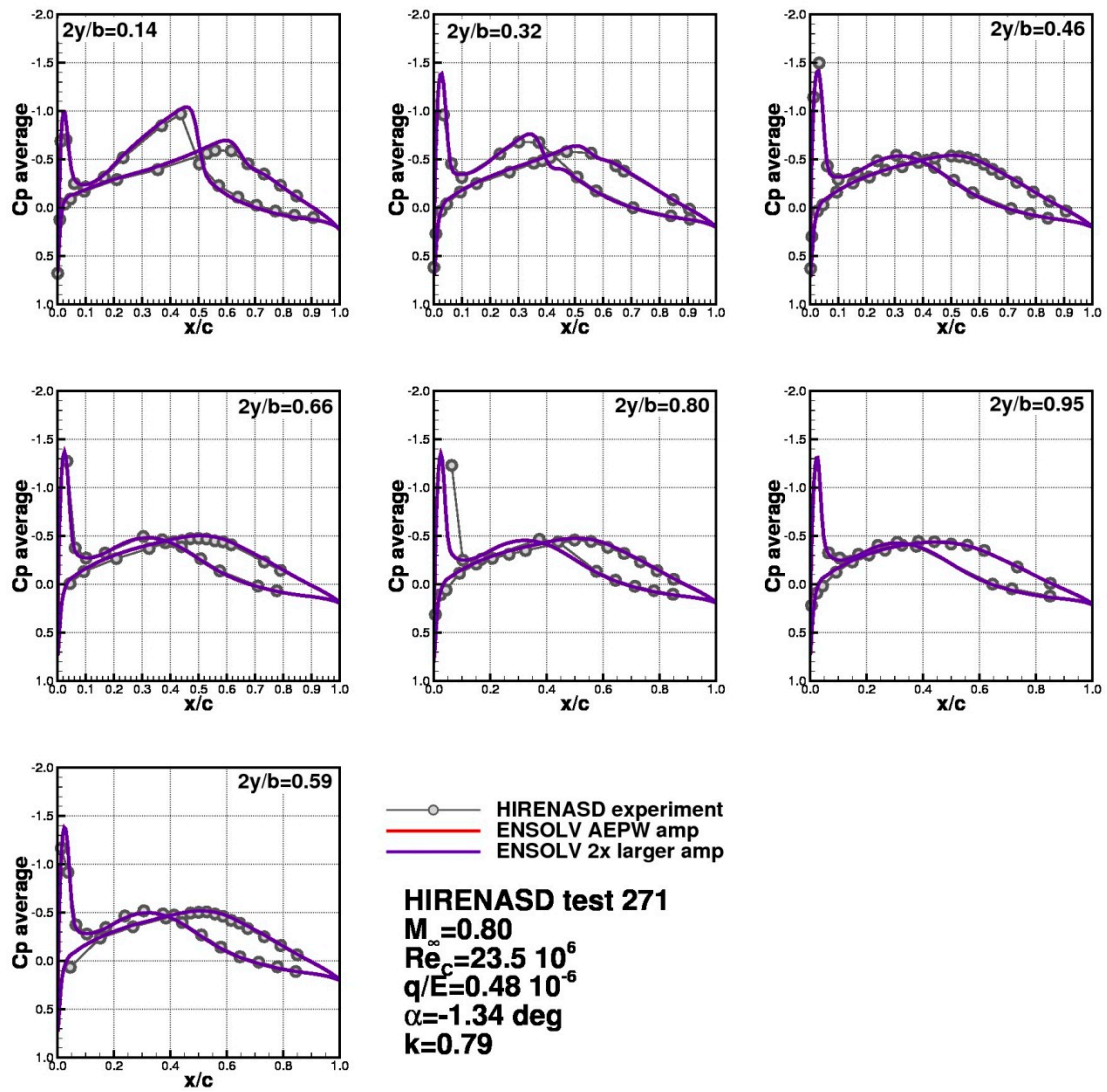


Figure 17 Comparison of the average pressure on the HIRENASD wing between computed and measured data for ETW271 test points of HIRENASD experiment for two amplitudes of oscillation

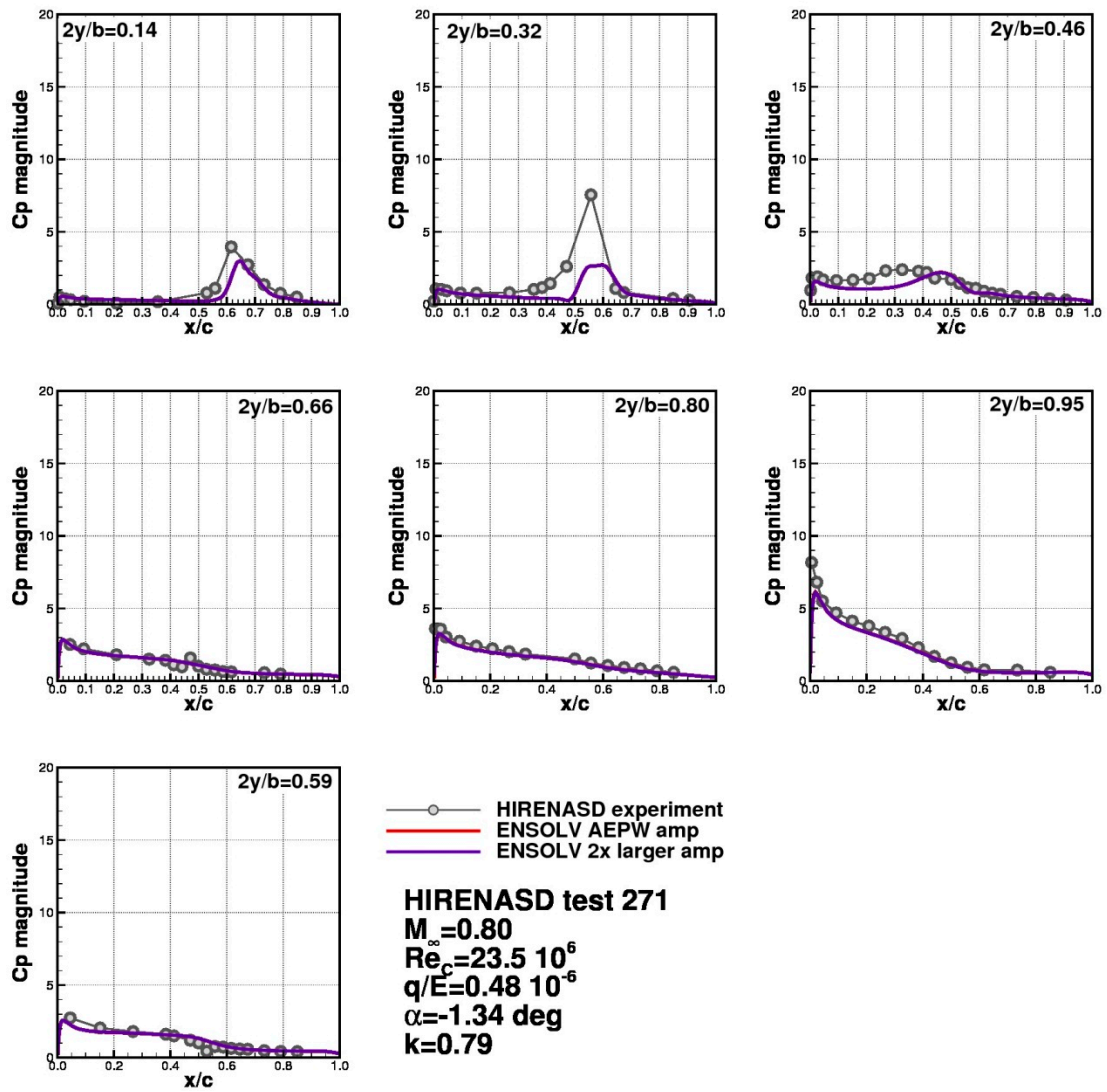


Figure 18 Comparison of the magnitude of unsteady pressure on the upper side of HIRENASD wing between computed and measured data for ETW271 test point of HIRENASD experiment for two amplitudes of oscillation.

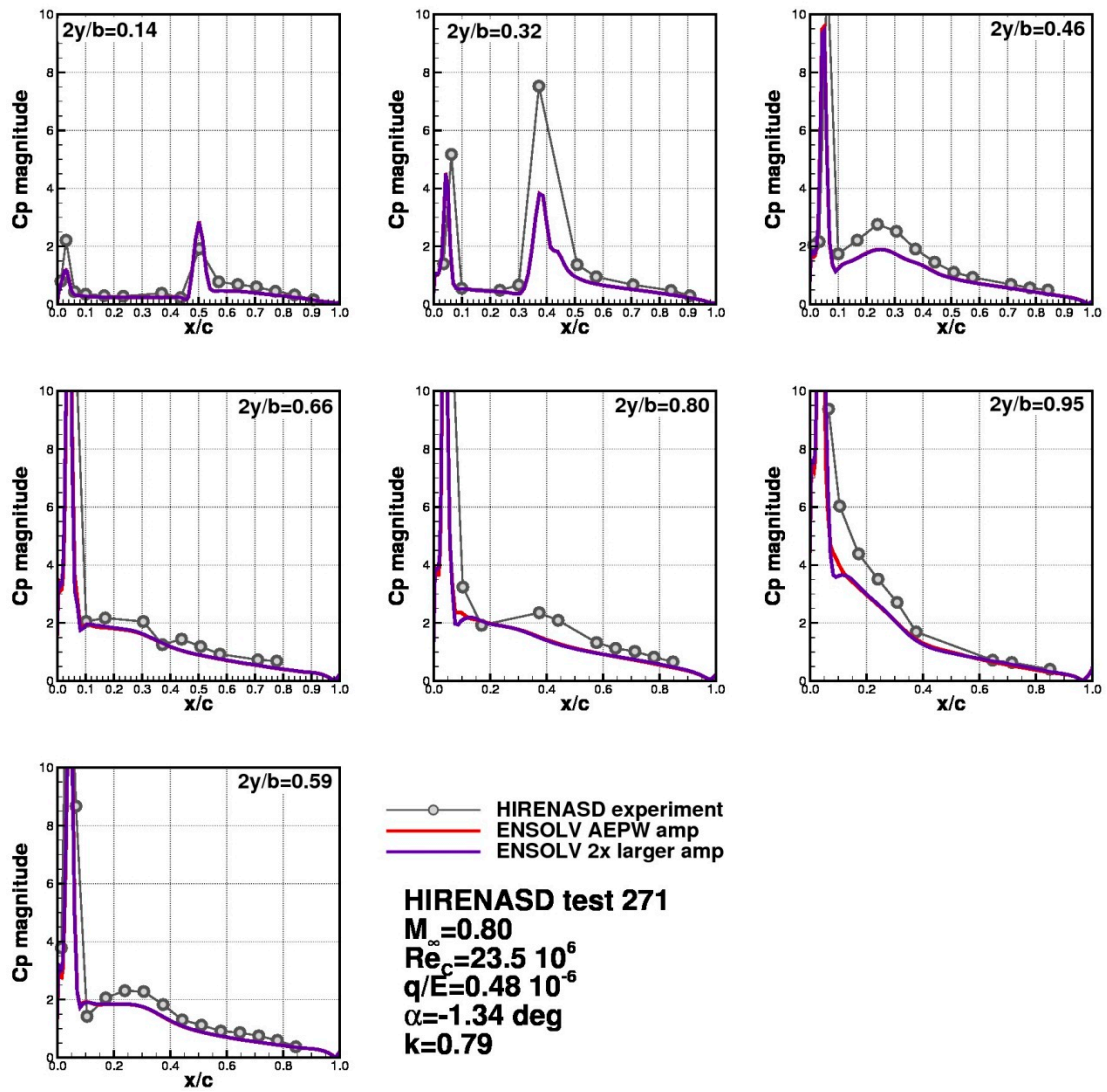


Figure 19 Comparison of the magnitude of unsteady pressure on the lower side of HIRENASD wing between computed and measured data for ETW271 test point of HIRENASD experiment for two amplitudes of oscillation.

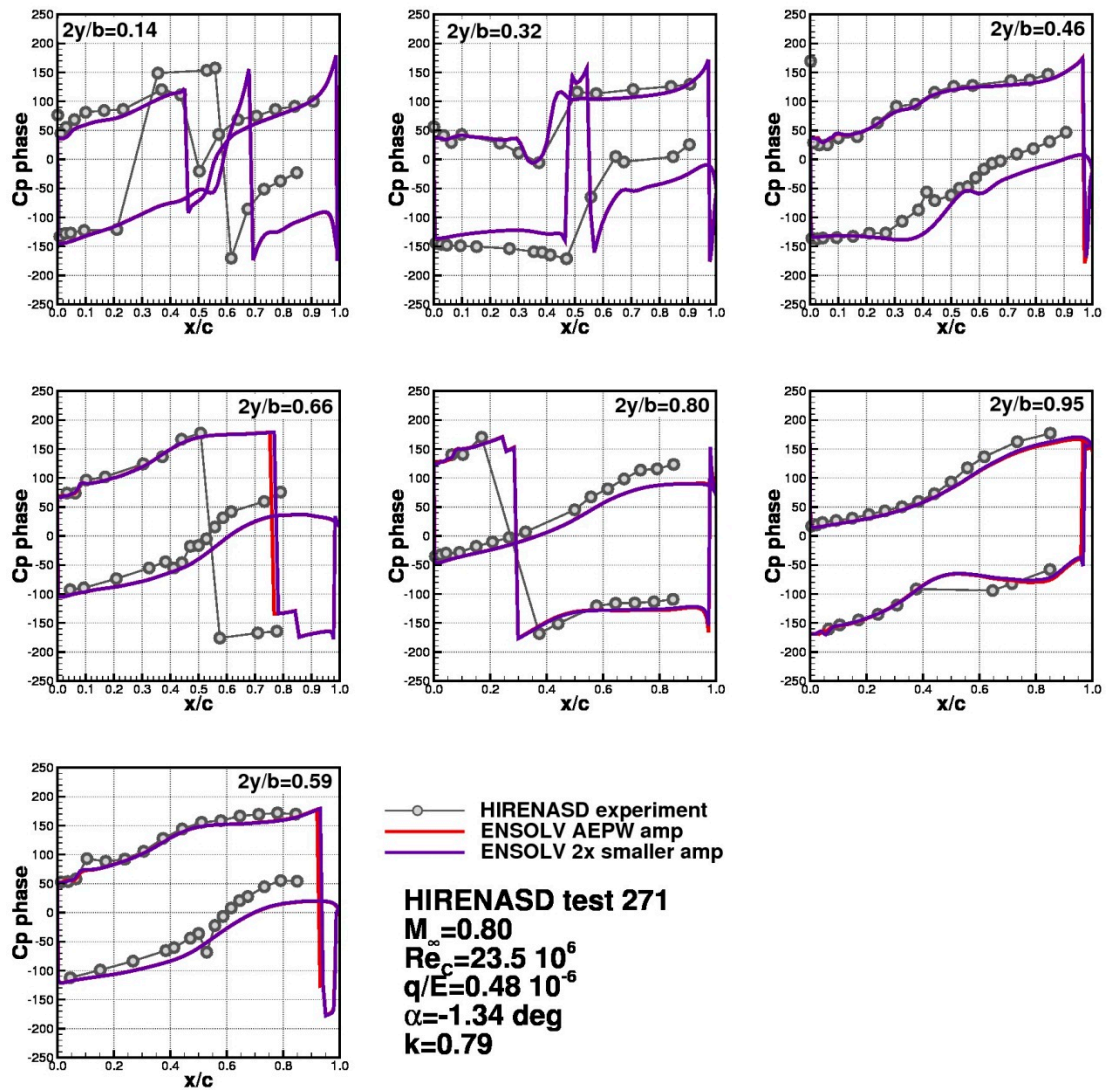


Figure 20 Comparison of the phase angle of unsteady pressure with respect to the motion of reference point on the HIRENASD wing between computed and measured data for ETW271 test point of HIRENASD experiment for two amplitudes of oscillation.

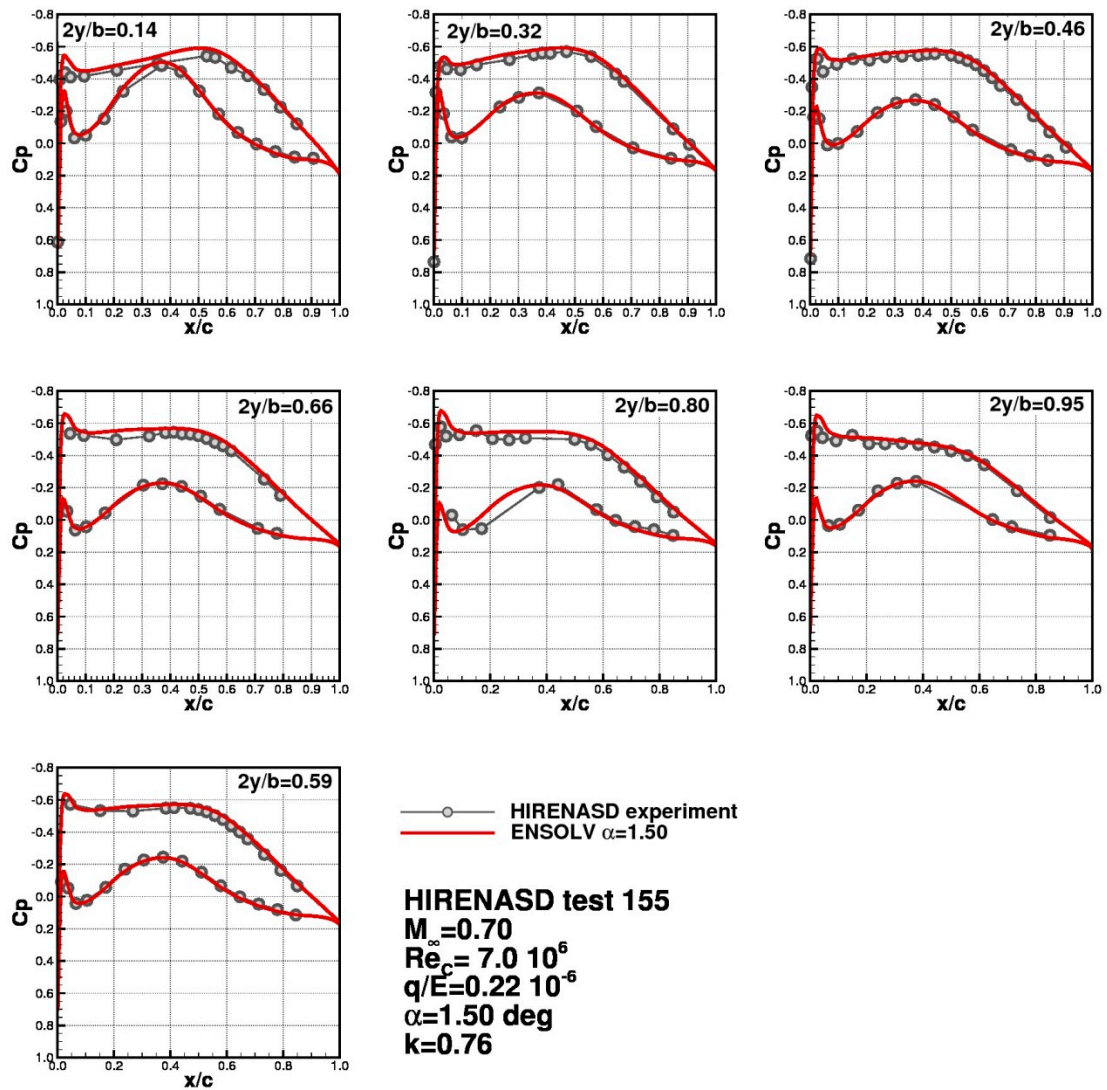


Figure 21 Comparison of the average pressure on the HIRENASD wing between computed and measured data for the optional case of ETW155 test points of HIRENASD experiment.

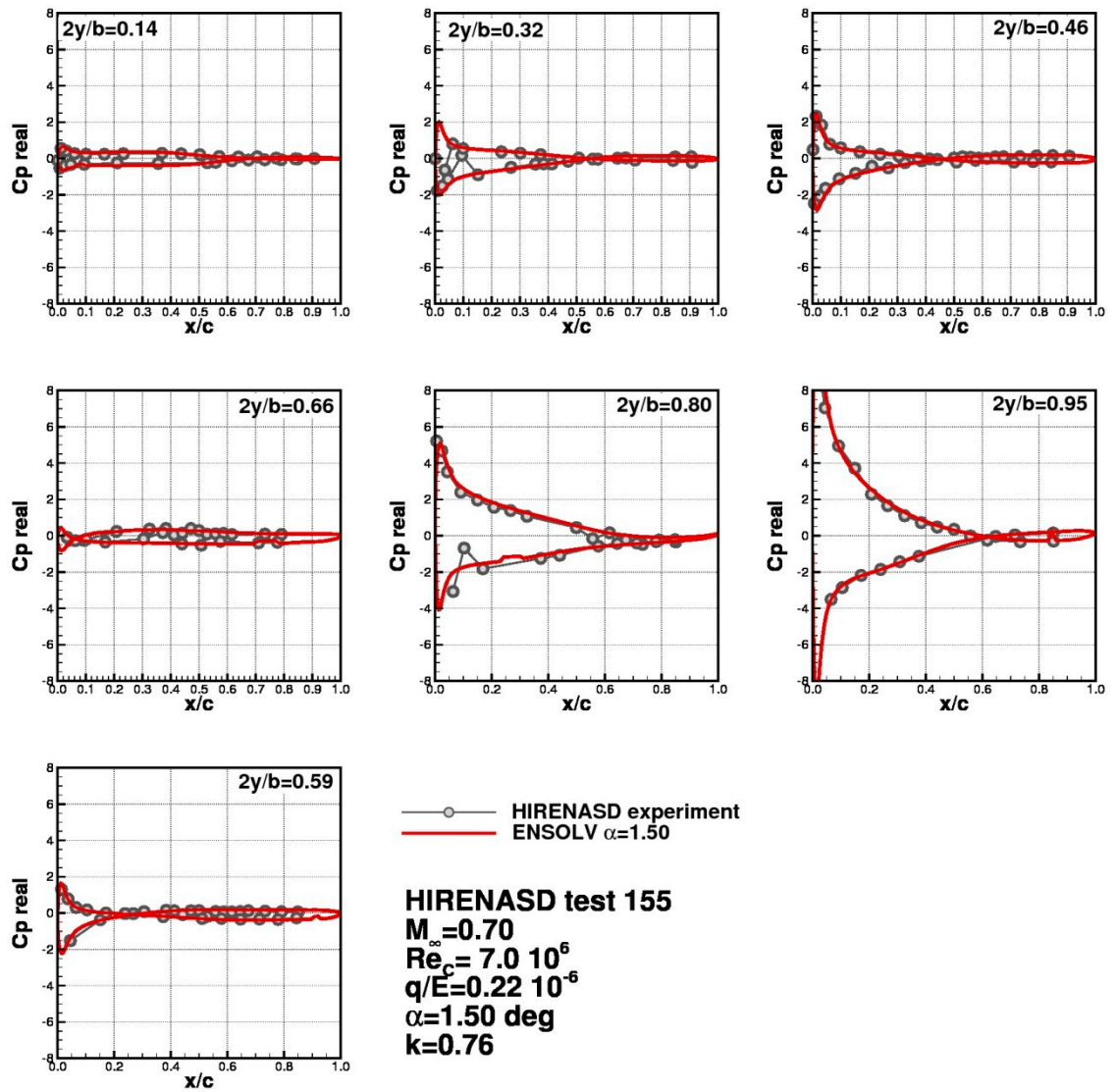


Figure 22 Comparison of the real part of unsteady pressure on the HIRENASD wing between computed and measured data for the optional case of ETW155 test points of HIRENASD experiment.

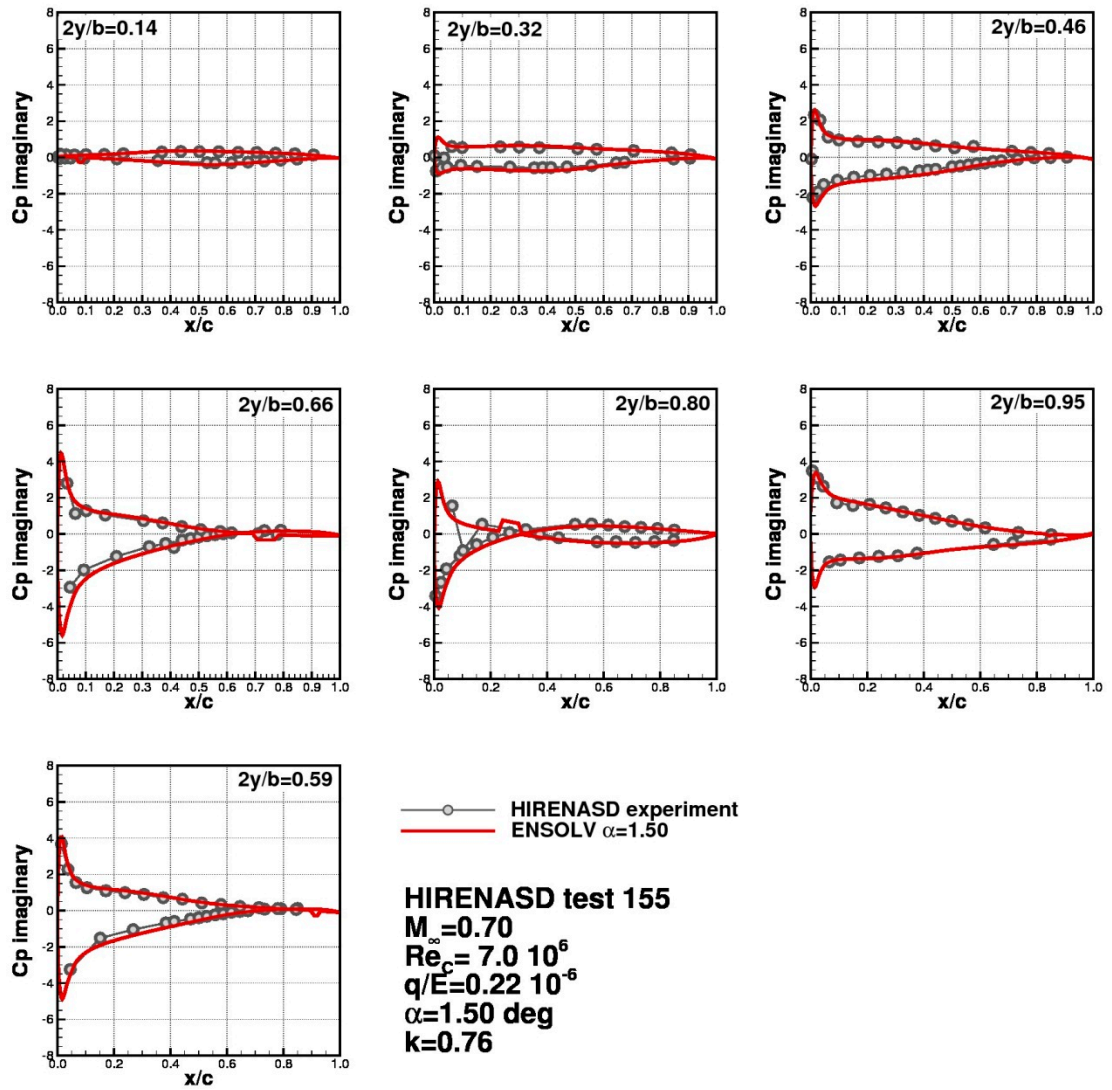


Figure 23 Comparison of the imaginary part of unsteady pressure on the HIRENASD wing between computed and measured data for the optional case of ETW155 test points of HIRENASD experiment

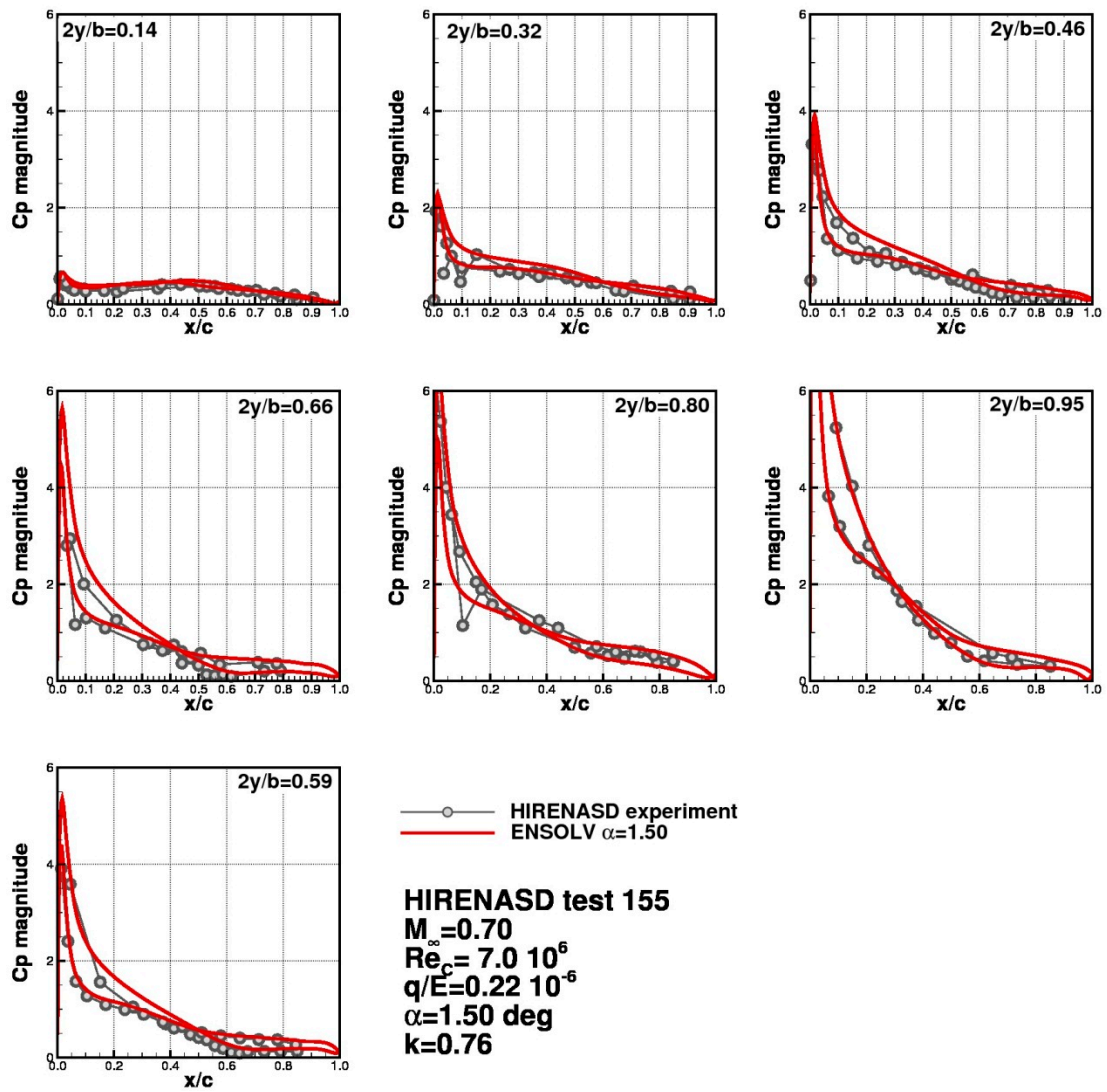


Figure 24 Comparison of the magnitude of unsteady pressure on the HIRENASD wing between computed and measured data for the optional case of ETW155 test points of HIRENASD experiment

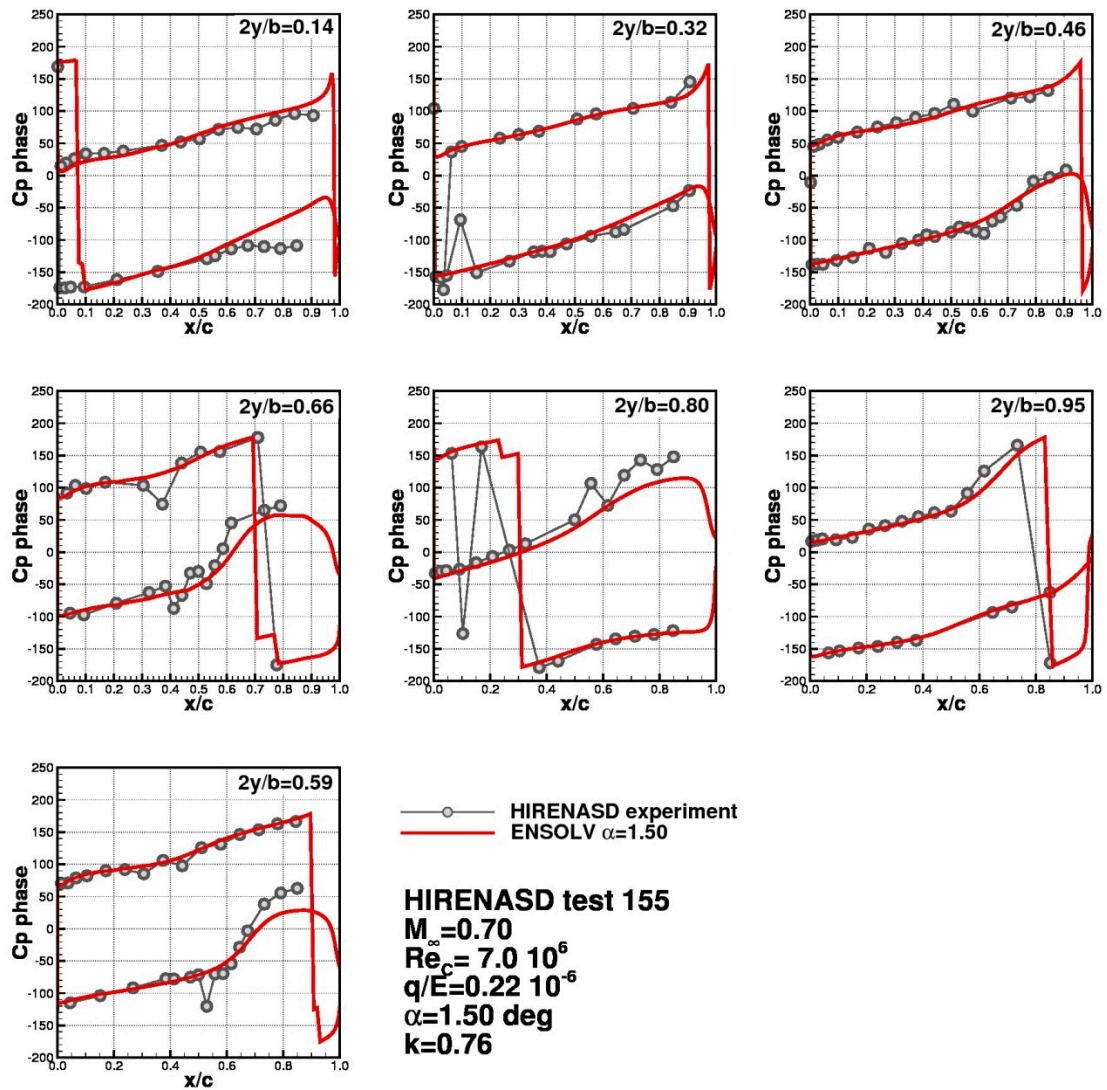


Figure 25 Comparison of the phase angle of unsteady pressure with respect to the motion of reference point on the HIRENASD wing between computed and measured data for the optional case of ETW155 test points of HIRENASD experiment

4 Conclusions

Results of simulations of the HIRENASD experiment for the vibration of the second bending mode are presented. The results constitute NLR's contribution to the First AIAA Aeroelastic Prediction Workshop. Based on the results, the following conclusions may be drawn:

1. Comparison of computed steady pressure and averaged pressure with the experimental data shows that the coupled CFD-CSM method properly captures the effect of static deformation instigating off-loading at the outer wing.
2. The phase angle between the pressure response and the motion of the reference point can in general be predicted with reasonable accuracy. Note, however that the location of the discontinuities in the phase angle distribution due to the shockwave travel, depends on the performance of the turbulence model in representing the shockwave-boundary layer interaction.
3. The magnitude of the pressure response is in general predicted slightly lower compared to the experimental data. This can be due to the fact that the experimental data is very noisy which influence the post-processing procedure in isolating the component with the frequency of interest. The computational results, on the other hand, are reasonably smooth.
4. The amplitude study shows that the unsteady part can be considered as a small perturbation about the average state, which is suitable for linearised methods.
5. In general, it can be concluded that the HIRENASD validation case has been successfully simulated and analysed using NLR in-house ENFLOW system.

To investigate the tendency of having too low magnitude of pressure compared to the experimental data, it is recommended to simulate the excitation mechanism of the HIRENASD experiment.

References

- [1] Rodden, W.P. and Johnson, E.H., MSC/NASTRAN Aeroelastic analysis users's guide version 68, MacNeal-Schwendler Corp, March 1994.
- [2] Ricketts, Sandford, Seidel, Watson. Transonic Pressure Distributions on a Rectangular Supercritical Wing Oscillating in Pitch, *Journal of Aircraft*, Vol 21 No 8, 1983.
- [3] David J. Piatak and Craig S. Cleckner. Oscillating Turntable for the Measurement of Unsteady Aerodynamic Phenomena. *Journal of Aircraft* Vol. 40, No. 1, January–February 2003
- [4] Prananta, B.B., Meijer, J.J. and van Muijden, J, Static aeroelastic simulation using CFD, comparison with linear method. Paper presented at International Forum on Aeroelasticity and Structural Dynamics 2003, Amsterdam, 2003.
- [5] Hounjet, M.H.L. and Meijer, J.J. Evaluation of elasto-mechanical and aerodynamic data transfer methods for non-planar configurations in computational aeroelastic analysis. Paper presented at International Forum on Aeroelasticity and Structural Dynamics 1995, Manchester, 1995.
- [6] Ballmann, J., Boucke, A., Reimer, L. and Dickopp, C., Results of dynamic experiments in the HIRENASD project and analysis of observed unsteady processes, International Forum on Aeroelasticity and Structural Dynamics, IFASD 2009-0103.
- [7] High Reynolds Number Aerostructural Dynamics (HIRENASD) at <http://heinrich.lufmech.rwth-aachen.de>.
- [8] AIAA Aeroelastic Prediction Workshop at <https://c3.nasa.gov/dashlink/projects/47>.
- [9] Ballmann, J. Experimental Analysis of high Reynolds Number structural Dynamics in ETW, 46th AIAA Aerospace Sciences Meeting and Exhibit, AIAA 2008-0841.
- [10] Moir, I.-R.M. Measurements on a two-dimensional aerofoil with high-lift devices. AGARD-AR-303, Vol. II, 58-59, 1994.
- [11] Prananta, B.B.; Veul, R.P.G., Houwink, R., Hounjet, M.H.L., Muijden, J. van, A generic flexible aircraft loads database system for fatigue analysis. Paper presented at International Forum on Aeroelasticity and Structural Dynamics 2007, Stockholm, Sweden.
- [12] J.C Kok, J.W. Boerstoel, A. Kassies, and S.P. Spekreijse. A robust multi-block navierstokesflow solver for industrial applications. NLR-TP-960503, NLR, Paper presented at Third ECCOMAS Computational Fluid Dynamics Conference, Paris, 1996
- [13] J.C. Kok. Resolving the dependence on freestream values for the $k-\omega$ turbulence model, *AIAA Journal*, Vol. 38, No. 7, pp. 1292-1295 (2000).
- [14] Spekreijse, Prananta, B.B. and Kok, J.C A simple, robust and fast algorithm to compute deformations of multi-block structured grids. NLR TP-2002-105, NLR.

- [15] B.B. Prananta, R.P.G. Veul and O.J. Boelens. Manoeuvre-loads computations using CFD-based static aeroelastic simulations for multiple store configurations. Proceedings of 27th International Congress of the Aeronautical Sciences, Nice, France, 2010. Paper 673.
- [16] R.J. Zwaan. Verification of calculation method for unsteady airloads in the prediction of transonic flutter. *AIAA Journal*. vol 22 no. 10, pp 833-839, 1985.
- [17] M.H.L. Hounjet and B.J.G. Eussen. Outline and application of the NLR aeroelastic simulation method. Proceedings of 19th Congress of ICAS, pp. 1418-1441, Anaheim, 1994.
- [18] H.S. Dol, J.C. Kok and B. Oskam. Turbulence modelling for leading-edge vortex flow. AIAA 2002-0843.
- [19] P. Bradshaw, D.H. Ferriss and N.P. Atwell. Calculation of boundary layer development using the turbulent energy equation. *Journal of Fluid Mechanics*, vol 28, pp 593-616, 1967.
- [20] F.R. Menter, Zonal two-equation $k-\omega$ turbulence models for aerodynamic flows. AIAA-93-2906, 1993.
- [21] D.A. Johnson and L.S. King. A new turbulence closure model for boundary layer flows with strong adverse pressure gradients and separation. AIAA 84-0175.

Acknowledgement

Part of the work carried out in the present project is funded by the Netherlands Ministry of Defence, through LCK2011/2012 programme. Part of the preliminary analysis was carried out during the investigation in European Union funded ALEF project, grant ACP7-GA-2009-211785 .

Appendix A Locations of accelerometers of HIRENASD wing

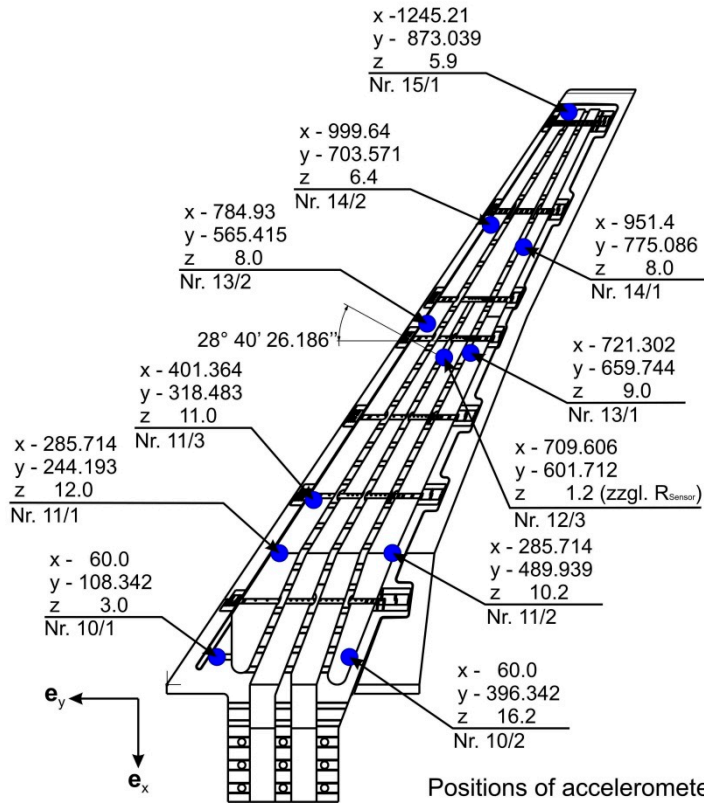


Figure A.1 Locations of the accelerometer of HIRENASD wing, Ref. [9]